Check for updates

Synthesis, multi-target evaluation and DFT analysis of 6-hydroxychromone derived hydrazones with carbonic anhydrase I–II/acetylcholinesterase inhibition and antioxidant activity

Wajeeha Zareen,[a] Nadeem Ahmed, [ID][b] Feyzi Sinan Tokali,[c] Talha Islam,[d] Mariya al-Rashida,[d] Ayşe Merve Senol, [ID][e] Orhan Ulucay,[f] Ahmed Mohamed Tawfeek,[g] Parham Taslimi,[h] Zahid Shafiq [ID] *[a] and Mohammad Shahidul Islam [ID] *[g]

Alzheimer's disease seems to be the result of several tumultuous processes such as cholinergic deficits associated with the abnormal metabolic status and oxidative stress that cannot be controlled effectively by single-target molecules. A complex group of agents capable of combining specific enzyme inhibition with antioxidant protection may be seen as an approach toward neuroprotection. The partial synthesis method led to the creation of a new series of chromone hydrazones (**3a–p**) from substituted hydrazones and 6-hydroxy-chromone. All the newly obtained hydrazones were assayed for their inhibitory activity against acetylcholinesterase (AchE) and human carbonic anhydrases (CA I and II), and their antioxidant potentials were also studied. The chromone-substituted hydrazones **3c**, **3e**, and **3f** exhibited good inhibitory activity against AChE with IC$_{50}$ values of 0.82 μM, 0.20 μM, and 1.11 μM, respectively. Compound **3e** was found to be highly selective for AChE and about six hundred fold more potent as compared to the standard inhibitor, tacrine. Also, these novel chromone derivatives were tested against CA I and II isoenzymes and exhibited IC$_{50}$ values within the range of 3.16 μM–19.28 μM against CA I and 1.21 μM–14.90 μM against CA II. In addition, *in vitro* antioxidant assays revealed that compounds **3c**, **3e**, and **3m** exhibited notable radical-scavenging activity, with compound **3e** showing superior antioxidant performance (IC$_{50}$ = 4.17 μg mL^{-1} for DPPH and 2.46 μg mL^{-1} for ABTS) compared to the reference standard trolox. Furthermore, cytotoxicity studies on HUVEC cells demonstrated that compounds **3c**, **3e**, and **3m** exhibited IC$_{50}$ values ranging from 52.36 to 60.84 μM. Molecular docking studies described the nature of binding affinities between the synthesized compounds and enzyme targets. DFT-based FMO, MEP, and reactivity analyses demonstrated that the chromone–hydrazone derivatives exhibit narrow HOMO–LUMO gaps and well-defined electrostatic surfaces, supporting their suitability for efficient charge transfer and biological interaction. Moreover, computational simulations and ADME analysis proved that all of the synthesized molecules were druggable with good inhibitory potential.

[a]Institute of Chemical Sciences, Bahauddin Zakariya University, Multan 60800, Pakistan. E-mail: zahidshafiq@bzu.edu.pk

[b]College of Chemistry & Chemical Engineering, Central South University, Changsha, Hunan 410083, China

[c]Department of Material and Material Processing Technologies, Kars Vocational School, Kafkas University, 36100 Kars, Turkey

[d]Department of Chemistry, Forman Christian College (A Chartered University), Ferozepur Road, 54600, Lahore, Pakistan

[e]Department of Medical Services and Techniques, Program of Medical Laboratory Techniques, University of Health Sciences, 34668, Istanbul, Turkey

[f]Department of Bioengineering, Faculty of Engineering and Architecture, Kafkas University, 36100 Kars, Turkey

[g]Department of Chemistry, College of Science, King Saud University, P. O. Box 2455, Riyadh 11451, Saudi Arabia. E-mail: mislam@ksu.edu.sa

[h]Department of Biotechnology, Faculty of Science, Bartin University, 74110 Bartin, Turkey

1 Introduction

Alzheimer's disease (AD), a chronic neurodegenerative disease, leads to progressive cerebral and neuropsychiatric failure and is responsible for nearly two-thirds of all dementia disorders.[1–3] Its growing pervasiveness and impact have encouraged researchers to design effective structures that decelerate or freeze its progression.[4] Targeting AChE, the enzyme responsible for breaking down the neurotransmitter acetylcholine (ACh), is one of the most promising therapeutic approaches.[5] AChE inhibition increases the ACh level in the brain, boosts cholinergic transmission and moderately compensates for neurodegeneration observed in AD.[6,7] Therefore, AChE inhibitors (AChEIs) have emerged as potential therapeutic agents, yet their observable side effects drive researchers to discover new scaffolds from organic sources.[8]

Being diuretic agents, carbonic anhydrase inhibitors (CAIs) find their applications for the prevention of a series of disorders such as angle-clouser glaucoma, pseudotumor cerebri and benign intracranial hypertension, pulmonary edema, seizure disorders, and in the treatment of high-altitude illness (HAI).[9–14] The inhibitory impacts of carbonic anhydrase include the lowering of concentration of bicarbonate ions (HCO_3^{-1}) reabsorption in the proximal convoluted tubule that is responsible for urinary basification and diuresis.[15–17] Furthermore, CAIs reduce not only aqueous humour production in the eye, which controls intraocular pressure, but also cerebrospinal fluid formation into the central nervous system (CNS).[18–20] Several carbonic anhydrase inhibitors are FDA-approved agents that are known for their primary as well as secondary mode of disease prevention.[21,22] Among them, Acetazolamide maintains the alkaline pH of urine which manage the level of uric acid or cystine stones.[23] The route of administration of CAIs involves oral, topical, intramuscular and intravenous, with precautionary measures recommended with nephric or hepatic dysfunctions.

The human brain is particularly vulnerable to oxidative stress, due to its high oxygen consumption and abundant content of polyunsaturated fatty acids in neuronal membranes.[24,25] In the context of Alzheimer's disease, excessive reactive oxygen species (ROS) generation, triggered by mitochondrial dysfunction, amyloid-β accumulation or metal dyshomeostasis, can lead to lipid peroxidation, protein and DNA oxidation, synaptic dysfunction and ultimately neuronal death.[26] As such, oxidative stress is considered not only a contributing factor to neurodegeneration, but also a possible early driver of pathological changes in AD.[27] Therefore, compounds possessing antioxidant (free radical scavenging) properties might help mitigate ROS-induced damage, protect neuronal integrity and slow down disease progression, representing a complementary neuroprotective strategy alongside classical enzyme-targeted interventions.

4-*H*-1-benzopyran-4-one (chromone) is a key heterocyclic nucleus that serves as a fundamental building unit in various medicinally potent natural as well as synthetic organic scaffolds.[28,29] Owing to structural adaptability, drug alikeness and interactions with a diverse range of biologically active binding sites, the chromone derivatives have long attracted the attention of synthetic chemists.[30] They are extensively studied for their broad range of pharmacodynamic applications, such as antimicrobial, neuroprotective, antitumour, antioxidant, antidepressant, antiviral, antidiabetic, and antiinflammatory potential.[30–37]

Hydrazones are bioisosteres of amides and imine and are synthesized by an acid condensation reaction between hydrazides and carbonyl compounds such as aldehyde and ketones.[38] The dynamic ligand–receptor affinities of these azomethine conjugates offer an extensive spectrum of pharmacological activities, including antitumor, anti-microbicidal, antiviral, anti-mycobacterial, antileishmanial, antiparkinson, anticonvulsant, antimalarial along with enzyme inhibition effects and menopausal hormone therapy.[39–48] Furthermore, hydrazidones act as a basic structural unit in several FDA-approved medications such as Gemtuzumab Ozogamicin and Inotuzumab Ozogamicin.

This study aims to design and evaluate multifunctional chromene–hydrazone derivatives as potential neuroprotective agents by simultaneously targeting key pathological mechanisms associated with Alzheimer's disease. To achieve this, the synthesized compounds were investigated for their inhibitory effects on AChE, which is directly implicated in cholinergic dysfunction, and CA I–II, which contribute to disrupted pH and ionic homeostasis during neurodegeneration. In parallel, their antioxidant activities were assessed using DPPH and ABTS assays, considering the critical role of oxidative stress in neuronal damage. By integrating enzyme inhibition profiles with radical-scavenging properties, this work aims to identify promising chemical scaffolds capable of addressing the multifactorial nature of Alzheimer's pathology.

2 Results and discussion

2.1. Chemistry

The series of chromone hydrazones (**3a–p**) was prepared by the treatment of 6-hydroxy-chromone-3-carbaldehyde with differently substituted hydrazides molecules (Fig. 1).

The structures of these synthesized derivatives were confirmed by using spectroscopic approaches such as ^{1}H NMR and ^{13}C NMR. The NMR spectra of prepared hydrazone chromones were recorded in DMSO-d$_6$ and reported with all possible assignments of protons (^{1}H) and carbons (^{13}C) within their expected ranges of chemical shifts. ^{1}H NMR spectrum of compounds **3a–p** generally consists of alkenyl Hs, aryl Hs and hetero protons' (OH and NH) signals. The characteristic resonance for amide NH was observed downfield at chemical shift of 12.00 ppm.[49,50] The protons related to aromatic nucleus appeared as multiplet within the range of 7.0–9.0 ppm. Moreover, the signal for characteristic azomethine proton (HC=N) appeared at chemical shift of 8.8–8.9 ppm.[51,52] In the ^{13}C NMR spectra of compounds, peaks of C=O carbons of hydrazide and chromene moieties are observed at δ 162–164 ppm and δ 175 ppm, respectively. Peaks of CH=N carbons appeared at δ 150 ppm.[53,54] To confirm the molecular formulas of new hydrazones, High-resolution mass spectrometry (HRMS) analysis was carried out. The experimentally observed molecular ion peaks were in excellent agreement with the calculated exact masses, supporting high purity and accurate elemental composition of the compounds. Owing to the presence of acidic OH group, main peak was observed for $[M - H]^+$ in most of the compounds, while in compound **3e**, major peak was observed as $[M + Na]^+$.

2.2. *In vitro* enzyme inhibition

The newly synthesized hydrazone derivatives in this study were investigated to evaluate their inhibitory properties against hCA I–II and AChE. The data obtained from the *in vitro* inhibition assays are presented in Table 1. Moreover, the kinetic studies identified the inhibition types of the compounds for all three enzymes. The Lineweaver–Burk plots can be found in the SI.
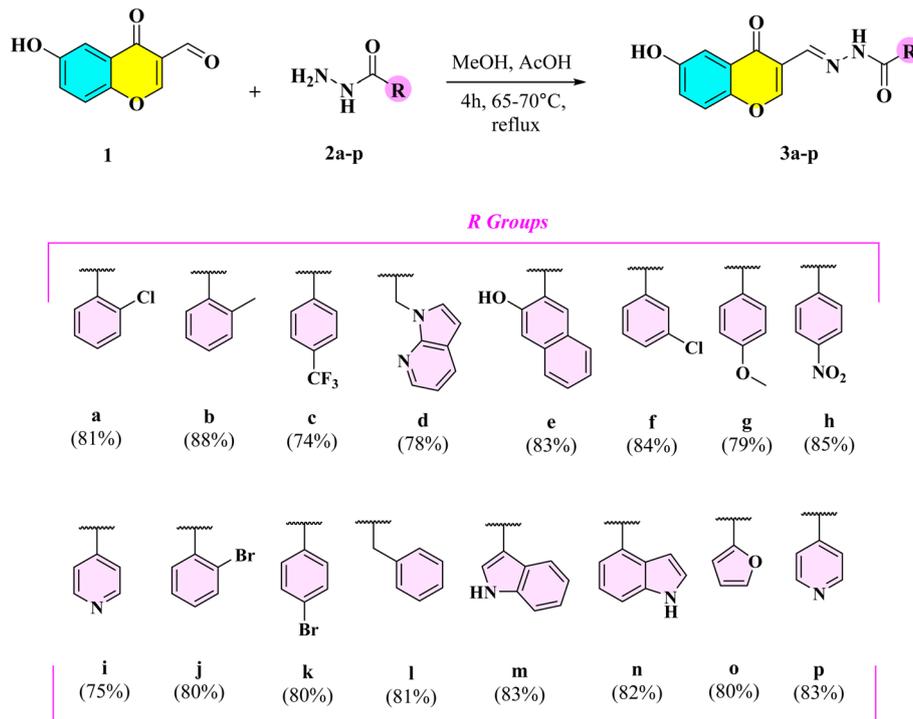
Fig. 1 Synthesis of compounds **3a–p**.

2.2.1 hCA I. For hCA I, the K_i values show a clear potency trend among the synthesized derivatives. Compounds **3c** (2.52 μM), **3e** (5.87 μM), and **3n** (5.61 μM) stand out as the most effective inhibitors, displaying substantially lower K_i values than the standard acetazolamide (AZA) (53.84 μM several additional derivatives, including **3o** (8.50 μM) and **3h** (5.50 μM), also exhibit strong activity, while the remaining compounds

show moderate inhibition. Most molecules outperform the reference, indicating that the series generally has good inhibitory potential toward hCA I. Additionally, the kinetic study revealed that compounds **3c**, **3e**, **3h**, **3j**, **3l**, **3m**, **3n**, and **3o** exhibit a competitive inhibition type.

2.2.2 hCA II. hCA II also exhibited a similar pattern in which most of the compounds showed stronger inhibition than

Table 1 *In vitro* inhibition results for hCA I–II, AChE and antioxidant activity

Comp.	IC$_{50}$ (μM)			K_i (μM)			Antioxidant IC$_{50}$ (μg mL^{-1})	
	hCA I	hCA II	AChE	hCA I	hCA I	AChE	DPPH	ABTS
3a	15.16 ± 1.01	11.46 ± 0.73	5.43 ± 0.04	19.16 ± 1.64	14.42 ± 1.06	2.54 ± 0.15	11.65 ± 0.24	5.73 ± 0.05
3b	18.71 ± 1.35	14.60 ± 0.98	3.65 ± 0.05	21.40 ± 2.28	20.35 ± 3.24	1.36 ± 0.10	9.41 ± 0.07	6.77 ± 0.86
3c	3.16 ± 0.02	1.21 ± 0.02	0.82 ± 0.01	5.87 ± 0.13	2.52 ± 0.21	0.75 ± 0.02	6.33 ± 0.02	5.01 ± 0.03
3d	15.34 ± 0.43	12.29 ± 0.35	4.27 ± 0.03	17.18 ± 3.47	14.02 ± 0.88	2.57 ± 0.13	8.02 ± 0.08	5.05 ± 0.08
3e	4.39 ± 0.05	2.46 ± 0.10	0.20 ± 0.01	6.14 ± 0.41	5.87 ± 1.50	0.08 ± 0.01	4.17 ± 0.02	2.46 ± 0.03
3f	11.08 ± 0.25	8.29 ± 0.44	1.11 ± 0.04	18.58 ± 2.87	12.21 ± 2.25	0.64 ± 0.05	8.54 ± 0.05	5.08 ± 0.05
3g	13.13 ± 0.07	10.75 ± 0.24	7.23 ± 0.10	20.06 ± 1.31	16.13 ± 1.06	4.76 ± 0.41	12.54 ± 1.01	6.52 ± 0.09
3h	10.56 ± 0.80	5.45 ± 0.50	4.86 ± 0.08	12.90 ± 2.05	5.50 ± 0.88	2.57 ± 0.66	10.98 ± 0.95	5.73 ± 0.08
3i	19.28 ± 0.98	14.90 ± 1.01	5.56 ± 0.12	25.41 ± 2.23	21.10 ± 3.55	3.61 ± 0.26	10.22 ± 0.07	6.87 ± 0.06
3j	8.31 ± 0.67	5.01 ± 0.09	3.03 ± 0.15	12.25 ± 1.31	11.27 ± 1.32	1.36 ± 0.03	8.57 ± 0.04	4.55 ± 0.13
3k	11.95 ± 0.20	7.32 ± 0.04	2.75 ± 0.06	14.15 ± 2.38	10.23 ± 1.44	1.06 ± 0.01	11.02 ± 0.91	4.62 ± 0.17
3l	15.70 ± 0.11	9.15 ± 0.22	6.48 ± 0.25	19.25 ± 3.51	13.80 ± 1.07	2.74 ± 0.04	7.94 ± 0.30	6.98 ± 0.23
3m	8.02 ± 0.03	7.29 ± 0.93	1.27 ± 0.03	12.48 ± 2.43	10.42 ± 0.74	0.68 ± 0.06	5.01 ± 0.08	4.06 ± 0.08
3n	5.14 ± 0.08	3.57 ± 0.05	0.85 ± 0.01	6.60 ± 0.16	5.61 ± 0.91	0.76 ± 0.01	13.75 ± 1.01	4.90 ± 0.03
3o	6.77 ± 0.21	5.41 ± 0.12	3.41 ± 0.06	9.61 ± 0.93	8.50 ± 0.84	1.47 ± 0.05	8.98 ± 0.06	5.67 ± 0.14
3p	8.63 ± 0.25	6.46 ± 0.28	1.36 ± 0.07	11.54 ± 1.02	8.92 ± 1.01	1.01 ± 0.02	9.04 ± 0.08	5.01 ± 0.06
AZA	50.47 ± 1.42	44.55 ± 3.04	—	64.57 ± 4.28	53.84 ± 4.86	—	—	—
TAC	—	—	12.43 ± 1.02	—	—	6.02 ± 0.70	—	—
Trolox	—	—	—	—	—	—	11.93 ± 0.70	5.98 ± 0.47

AZA (64.57 μM). The most potent derivatives **3c** (5.87 μM), **3e** (6.14 μM), and **3n** (6.60 μM) are also low-K_i type reflecting a high potency in this isoform of the enzyme. Other notable active compounds are **3h** (12.90 μM) and **3o** (9.61 μM) which are pretty strong too. It has been shown that the series has several different members which are still extremely effective against both hCA isoforms. Also, the kinetic study data confirmed that the inhibitors **3c**, **3e**, **3h**, **3j**, **3n**, and **3o** belong to the group of competitive inhibition.

2.2.3 AChE. In terms of AChE inhibition, the compounds have a very wide range of activities and many derivatives have very strong potency. The most impressive is **3e** ($K_i = 0.08$ μM), which is extremely more potent than the reference drug tacrine (6.02 μM). The list of other highly potent examples is completed by **3f** (0.64 μM), **3c** (0.75 μM), and **3n** (0.76 μM). Even the moderately active compounds usually have lower K_i values compared to the standard, which means that the series has overall strong cholinesterase inhibitory capacity, with some derivatives showing submicromolar effectiveness. All compounds show a competitive inhibition type with respect to AChE. The substantially lower IC_{50} value of compound **3e** compared to tacrine indicates a markedly higher inhibitory potency toward AChE. This suggests that effective enzyme inhibition may be achieved at much lower concentrations. Such a difference is particularly relevant, as tacrine is known to cause dose-dependent adverse effects, including hepatotoxicity. Therefore, the enhanced potency of compound **3e** may represent an advantage by potentially allowing reduced dosing while maintaining efficacy.

The structure–activity relationship (SAR) analysis of novel chromone hydrazones exhibits detail information about their inhibitory impacts against hCA I–II and AChE. The IC_{50} values of compounds **3c** (3.16 and 1.21 μM), **3e** (4.39 and 2.46 μM), and **3n** (5.14 and 3.57 μM) exhibit significant inhibition, whereas compounds like **3a** (15.16 and 11.46 μM), **3b** (18.71 and 14.60 μM), **3i** (19.28 and 14.90 μM), and **3l** (15.70 and 9.15 μM) indicate slightly lower inhibition effect among all derivatives. Again,

the inclusion of hydroxy naphthol and trifluoromethyl phenyl groups at favorable places on the hydrazone seems to boost binding affinity for hCA I and II targets. The good inhibition potential of compounds **3c** (0.82 μM), **3e** (0.20 μM), **3f** (1.11 μM), **3m** (1.27 μM), **3n** (0.85 μM), and **3p** (1.36 μM) against AChE is confirmed by their lower IC_{50} values. The presence of trifluoromethyl phenyl, hydroxy naphthol groups, chlorophenyl, indolyl group and pyridine groups in these compounds respectively, seems to enhance their inhibitory actions. The most potent AChE inhibition is done with compound **3e** containing a hydroxy group at position 2 and both **3c** and **3n** following closely behind. Though all the compounds are potentially active when compared with reference but the compounds **3g** and **3l** display reduced inhibitory effects against AChE because their non polar substituents create weak interactions that are responsible for achieving proper alignment or mobility required for successful binding events. Binding and inhibitory efficiency towards AChE drops for the 2-chlorophenyl and pyridinyl groups because they experience both structural blocking effects and fewer beneficial molecular interactions within the enzyme complex (Fig. 2).

2.3. Antioxidant activity

The synthesized hydrazone derivatives were assayed for their antioxidant potential by means of two complementary *in vitro* tests, DPPH and ABTS, which were used to evaluate their ability to scavenge free radicals. The data showed significant differences in the activity of the compounds series that made it possible to distinguish very well the most active substances in every test (Table 1).

2.3.1 DPPH. The DPPH scavenging assay revealed that a few derivatives were very effective antioxidants, having IC_{50} values lower than that of the standard trolox (11.93 μg mL^{-1}). Among them, **3e** (4.17 μg mL^{-1}), **3m** (5.01 μg mL^{-1}), and **3c** (6.33 μg mL^{-1}) were the most active in the series. Compounds **3n** (13.75 μg mL^{-1}) and **3g** (12.54 μg mL^{-1}) were also moderately active scavengers, while the other derivatives had quite low
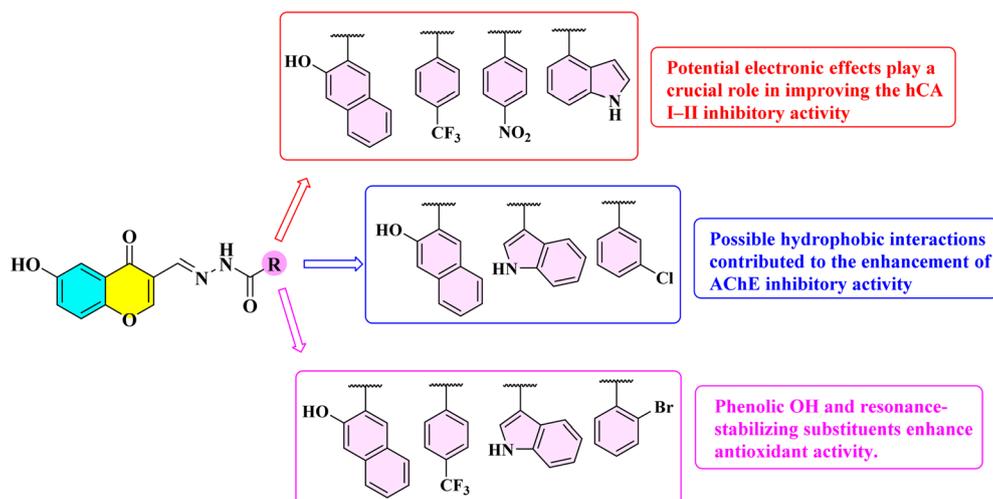

Fig. 2 The SAR analysis of new chromone derivatives.
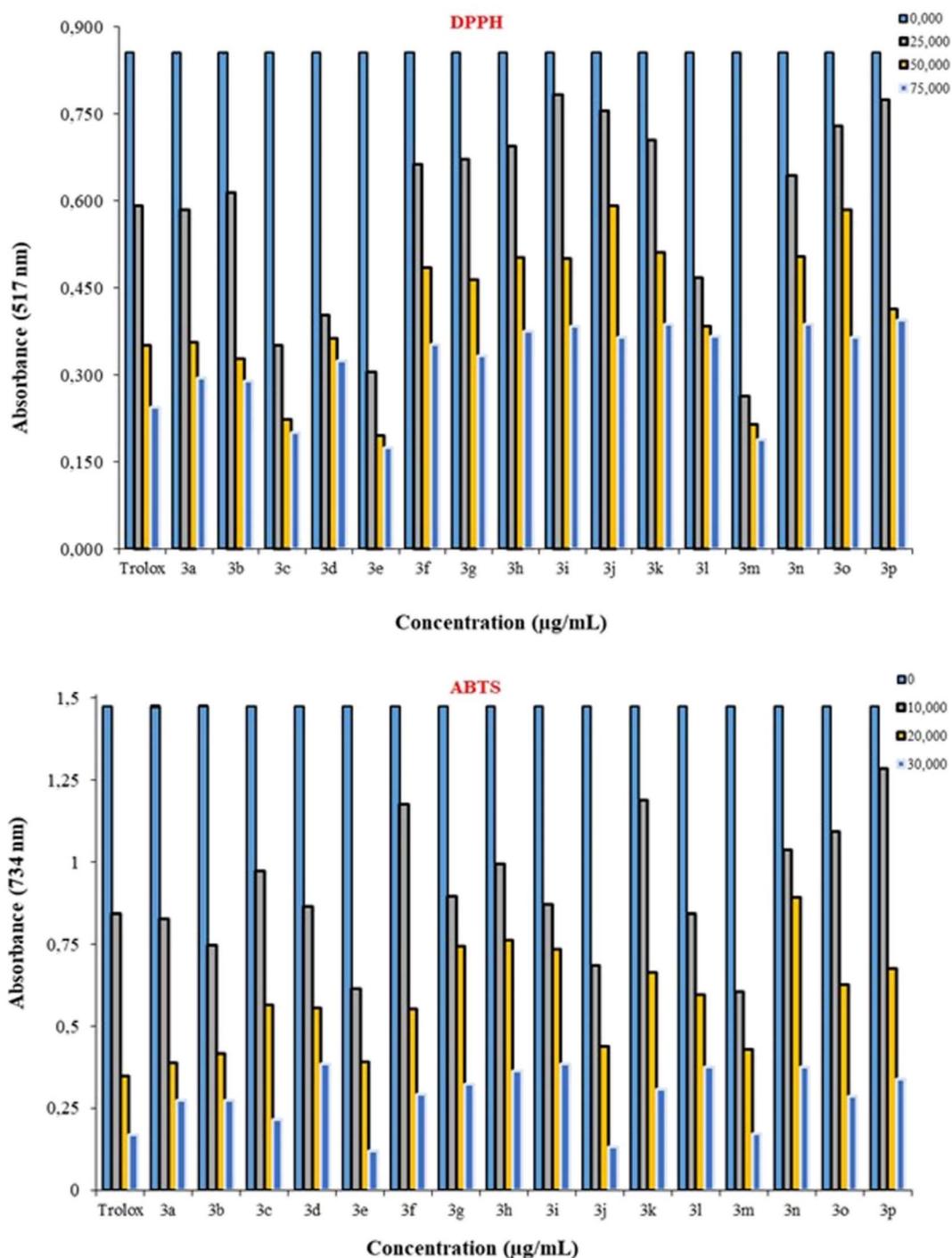
Fig. 3 Antioxidant activity graphs of compounds 3a–p.

Table 2 Cytotoxic effects of the most active compounds against HUVEC cell line

Compounds	HUVEC IC$_{50}$ [μM]
3c	58.51 ± 2.85
3e	60.84 ± 2.76
3m	52.36 ± 3.12

activities. The DPPH results indicate that a portion of the series is capable of strong radical-quenching (Fig. 3).

2.3.2 ABTS. The ABTS results generally followed a similar trend, with several compounds displaying IC$_{50}$ values comparable to or better than trolox (5.98 μg mL^{-1}). The most effective derivatives were **3e** (2.46 μg mL^{-1}), **3m** (4.06 μg mL^{-1}), and **3j** (4.55 μg mL^{-1}), all showing strong activity. Many other compounds, including **3c** (5.01 μg mL^{-1}), **3p** (5.01 μg mL^{-1}),

Fig. 4 Overlap of docked conformations of hCA I inhibitors with the co-crystallized inhibitor (represented in black).

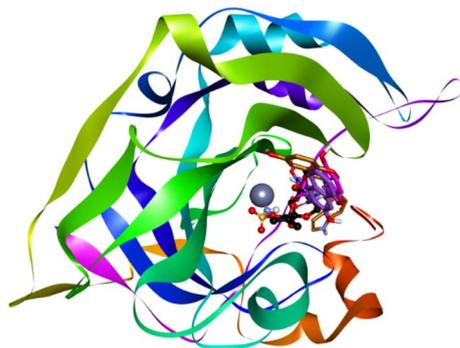and **3o** (5.67 μg mL^{-1}), also performed well, indicating broad antioxidant capacity across the series. A few derivatives showed weaker effects, but the majority demonstrated meaningful ABTS scavenging efficiency (Fig. 3).

For antioxidant activities, IC$_{50}$ values from DPPH and ABTS assays substances are taken as evidence. Compounds **3c** and **3e**, contain trifluoromethyl phenyl and hydroxy naphthol, indicating that this substitution decreases the reactivity of free radicals by stabilizing them within living structures. In contrast,

substances like **3g** and **3n** exhibit lesser inhibition, confirming the hypothesis that hydroxy naphthol and trifluoromethyl phenyl improve antioxidant potential of synthesized compounds (Fig. 2). The superior antioxidant activity of compound **3e** in both DPPH and ABTS assays can be attributed to the presence of the 2-naphthol moiety, which contains a phenolic hydroxyl group. Phenolic OH groups are well known for their ability to donate hydrogen atoms to neutralize free radicals, forming relatively stable phenoxyl radicals. Moreover, the extended aromatic naphthol system allows effective delocalization of the unpaired electron through resonance, further stabilizing the radical species and enhancing overall scavenging efficiency.

2.4. Cytotoxicity

In line with the *in vitro* enzyme inhibition and antioxidant activity findings, the cytotoxic effects of the most promising compounds in the series (**3c**, **3e**, and **3m**) were assessed on the healthy human endothelial cell line (HUVEC). The results are summarized in Table 2.

The tested compounds exhibited moderate cytotoxicity against HUVEC cells, with IC$_{50}$ values ranging between approximately 52–61 μM. Importantly, these IC$_{50}$ values are substantially higher than the concentrations required for

Table 3 Details of binding site interactions of docked conformation of hCA I inhibitors **3c**, **3e** and **3n**

| Code	Interactions	Type	Distnace (Å)
3c	SER65:HG – lig:F1	Hydrogen bond; halogen (fluorine)	2.94
	SER65:HG – lig:F4	Hydrogen bond; halogen (fluorine)	2.76
	ASN69:HD21 – lig:O38	Hydrogen bond	3.02
	GLN92:HE22 – lig:O16	Hydrogen bond	1.75
	HIS64:CD2 – lig:F4	Carbon hydrogen bond	2.76
	SER65:CB – lig:F4	Carbon hydrogen bond	2.55
	HIS67:CE1 – lig:O38	Carbon hydrogen bond	2.55
	HIS94:CD2 – lig:F1	Carbon hydrogen bond	3.31
	HIS96:CE1 – lig:F1	Carbon hydrogen bond	2.42
	HIS96:CE1 – lig:F3	Carbon hydrogen bond	2.83
	PHE95:O – lig:F1	Halogen (fluorine)	3.44
	HIS96:NE2 – lig:F1	Halogen (fluorine)	2.90
	HIS64:HE2 – lig	Pi–donor hydrogen bond	3.12
	Lig:F1 – HIS96	Pi–lone pair	2.89
	HIS94 – lig	Pi–pi stacked	3.87
	HIS64 – lig:C2	Pi–alkyl	4.59
	HIS94 – lig:C2	Pi–alkyl	4.77
	HIS96 – lig:C2	Pi–alkyl	3.93
3e	Lig:H37 – PHE95:O	Hydrogen bond	2.73
	GLN92:HE22 – lig:O42	Hydrogen bond	2.48
	HIS67:CD2 – lig:O42	Carbon hydrogen bond	2.74
	HIS94:CD2 – lig:O36	Carbon hydrogen bond	2.92
	ZN261:ZN – lig	Pi–cation	4.80
	HIS64:HE2 – lig	Pi–donor hydrogen bond	2.56
	HIS64 – lig	Pi–pi T-shaped	4.42
	HIS200 – lig	Pi–pi T-shaped	4.94
	Lig – LEU131	Pi–alkyl	4.82
3n	Lig:H2 – PHE91:O	Hydrogen bond	1.70
	Lig:H29 – PRO201:O	Hydrogen bond	1.75
	GLN92:HE22 – lig:O19	Hydrogen bond	3.02
	ASP72:OD1 – lig	Pi–anion	4.80

Paper
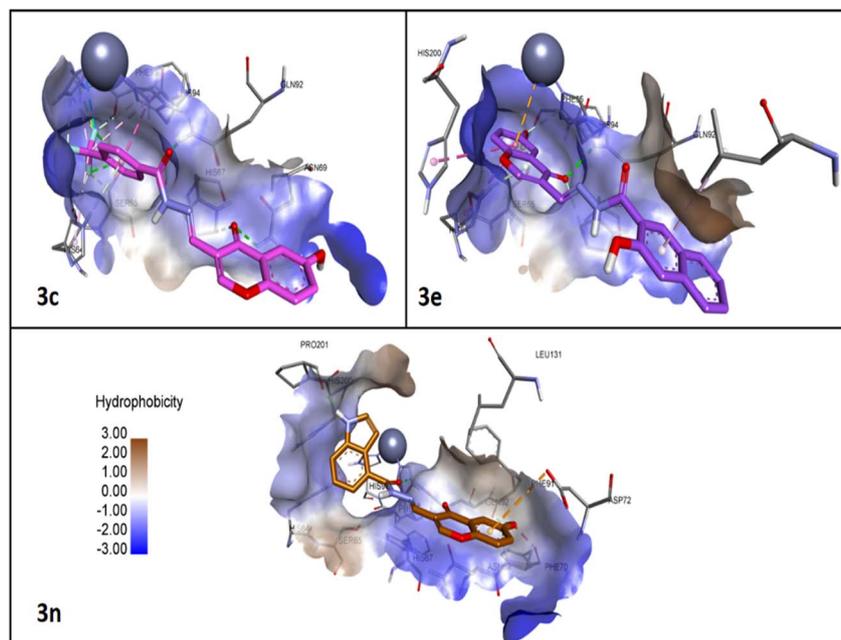
Fig. 5 Binding interactions of docked conformations of hCA I inhibitors with surface representation.

enzyme inhibition, suggesting that the most active derivatives display a favorable preliminary safety margin *in vitro*. The corresponding dose–response curves are provided in the SI.

2.5. Molecular docking

2.5.1 Molecular docking studies of hCA I inhibitors. The crystal structures of hCA I and hCA II (PDB ID: 3lxe and 1a42, respectively) and hAChE (PDB ID: 4m0e) were downloaded from the rcsb.org. Molecular docking studies of three most active inhibitors of hCA I (**3c**, **3e** and **3n**) revealed that all compounds bind in the same region of the active site as the co-crystallized inhibitor, near the active site's metal (zinc) center (Fig. 4 and Table 3).

The amino acid Gln92 is near the entrance of the active site cleft in hCA I. Hence, hydrogen bond interaction with Gln92 appears to be important for inhibition of these compounds as all three compounds **3c**, **3e** and **3n** were found to make hydrogen bond with this amino acid. In compounds **3c** and **3n**, it was the carbonyl oxygen of the amide group, while in **3n** the carbonyl of chromone ring was making hydrogen bond with Gln92. Other amino acids repeatedly involved in hydrogen bonded interactions, including carbon hydrogen bonds were found to be His64, His67, His94 and His96 (Table 3), all of which are present at the lining of the active site cavity. His64 is also a critical amino acid involved in "histidine proton shuttle" mechanism and helps to stabilize the substrate for catalysis. His94 and His96 are directly involved in coordinating the active site's zinc metal ion, and are therefore crucial for maintaining the integrity of coordination geometry around the divalent zinc metal ion. In **3c** the trifluoromethyl group was making a carbon hydrogen bond with Ser65, and halogen bonds with Ser65 and Phe95. In compound **3e**, Phe95 and His94 were making

hydrogen bond and carbon hydrogen bond with the OH group substituted on the chromone ring (Fig. 5).

The aromatic rings of the ligand are stabilized by pi interactions. His94, and His64 and His200 were making pi–pi stacking and pi–pi T-shaped interactions with the phenyl and chromone rings of **3c** and **3e** respectively. The only interaction with the active site's zinc metal ion was a pi–cation interaction with the chromone ring of compound **3e**. In compounds **3c** and **3e**, pi–alkyl interactions were observed with His94, His96, and Leu131.

2.5.2 Molecular docking studies of hCA II inhibitors. Compounds **3c**, **3e** and **3h** were the most active inhibitors of hCA II, and were therefore selected for molecular docking studies. All compounds were found in the active site with similar orientations (Fig. 6). One of the most characteristic

Fig. 6 Overlap of docked conformations of hCA II inhibitors with the co-crystallized inhibitor (represented in black).
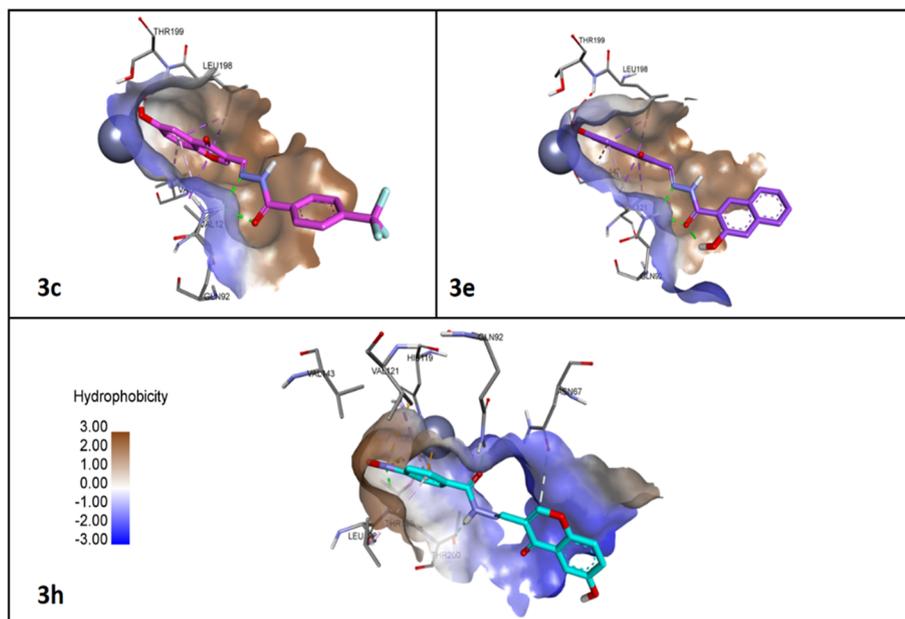
Fig. 7 Binding interactions of docked conformations of hCA II inhibitors with surface representation.

binding features observed for these inhibitors was the ligand coordination with the active site's zinc metal ion. For compounds **3c** and **3e** the oxygen atom of the hydroxyl group

Table 4 Details of binding site interactions of docked conformation of hCA II inhibitors **3c**, **3e** and **3h**

Code	Interactions	Type	Distnace (Å)
3c	GLN92:HE22 – lig:O16	Hydrogen bond	2.11
	GLN92:HE22 – lig:N19	Hydrogen bond	2.15
	ZN262:ZN – lig:O32	Metal–acceptor	1.90
	VAL121:CG2 – lig	Pi–sigma	3.78
	LEU198:CD2 – lig	Pi–sigma	3.24
	LEU198:CD2 – lig	Pi–sigma	3.84
	Lig – VAL121	Pi–alkyl	4.88
	Lig – VAL143	Pi–alkyl	4.91
3e	Lig:H2 – lig:O20	Hydrogen bond	1.94
	GLN92:HE22 – lig:O20	Hydrogen bond	2.14
	GLN92:HE22 – lig:N23	Hydrogen bond	2.26
	ZN262:ZN – lig:O36	Metal–acceptor	1.82
	VAL121:CG1 – lig	Pi–sigma	3.91
	VAL121:CG2 – lig	Pi–sigma	3.85
	LEU198:CD2 – lig	Pi–sigma	3.18
	LEU198:CD2 – lig	Pi–sigma	3.86
	Lig – VAL121	Pi–alkyl	4.92
	Lig – VAL143	Pi–alkyl	4.89
3h	Lig:N2 – GLU106:OE1	Attractive charge	5.53
	ZN262:ZN – lig:O3	Attractive charge	3.83
	Lig:H17 – THR200:OG1	Hydrogen bond	2.14
	GLN92:HE21 – lig:O15	Hydrogen bond	1.99
	THR199:HN – lig:O3	Hydrogen bond	2.12
	Lig:C22 – ASN67:OD1	Carbon hydrogen bond	3.40
	ZN262:ZN – lig	Pi–cation	3.72
	Lig:O3 – HIS119	Pi–anion	4.56
	Lig – VAL121	Pi–alkyl	5.42
	Lig – LEU198	Pi–alkyl	4.78

substituted on the chromone ring was in contact with the zinc metal ion, whereas for compound **3h** it was the nitro group oxygen that was making contact with the zinc metal ion; additionally, a pi–cation was also observed between zinc metal ion and the phenyl ring of **3h.** One of the most important hydrogen bonded interactions observed for all three compounds was with Gln92 (one of the most conserved amino acid residues among CA isozymes), here the amide linking group of inhibitors was making hydrogen bonds with Gln92.

The amino acids Val121, Leu198 and Val143 are part of the hydrophobic sub-pocket near the active site, the hydrophobic part of the molecules in **3c**, **3e** and **3h** were stabilized in this region *via* hydrophobic pi–alkyl and pi–sigma interactions with these amino acids (Fig. 7) (Table 4).

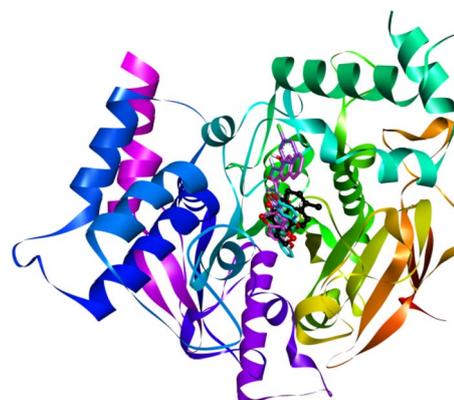**2.5.3 Molecular docking studies of AChE inhibitors.** Several hydrogens bonded interactions were observed in

Fig. 8 Overlap of docked conformations of AChE inhibitors with the co-crystallized inhibitor (represented in black).

© 2026 The Author(s). Published by the Royal Society of Chemistry

docking studies of most active AChE inhibitors **3e**, **3f** and **3m** (Fig. 8). In compound **3m**, the NH group of the indole ring was making hydrogen bonds with His447 and Ser203, both these amino acids are part of the catalytic triad of the enzyme, hence engagement of these amino acids by the inhibitors is important for its inhibition. The chromone ring carbonyl group and the OH group substituted on the chromone ring were making hydrogen bonds with Phe295 and Ser293 respectively. The –C=N– group was making a carbon–hydrogen bond with Tyr124. In compound **3e**, the OH group of naphthyl ring was making hydrogen bond with Gln91, while the carbonyl oxygen was making a hydrogen bond with Ser293 and the chromone ring oxygen was making a hydrogen bond with Phe295. In **3e** the NH group was making a hydrogen bond with Gln91 Table 5.

Hydrophobic π interactions are crucial for stabilizing the aromatic rings of the inhibitors. Repeated π interactions (π–π stacked) were observed for chromone ring of all compounds with Trp341 and Trp286 (key amino acids in the active site gorge). In compound **3m**, Trp86 was making π–π T-shaped interaction with the indole ring. The naphthyl ring of **3e** was also making a π–π T-shaped interaction with His287. For compounds **3e** and **3f**, pi–anion interactions with Glu292 contributed to electrostatic stabilization of the inhibitor

Table 5 Details of binding site interactions of docked conformation of AChE inhibitors **3e**, **3f** and **3m**

Code	Interactions	Type	Distnace (Å)
3e	Lig:H2 – GLN291:O	Hydrogen bond	1.98
	SER293:HN – lig:O20	Hydrogen bond	1.84
	SER293:HG – lig:O20	Hydrogen bond	2.59
	PHE295:HN – lig:O29	Hydrogen bond	2.26
	GLU292:OE2 – lig	Pi–anion	3.99
	Lig – TRP286	Pi–pi stacked	5.44
	Lig – TYR341	Pi–pi stacked	4.43
	Lig – TYR341	Pi–pi stacked	3.81
	HIS287 – lig	Pi–pi T-shaped	5.20
	Lig – VAL294	Pi–alkyl	5.38
3f	Lig:H15 – GLN291:O	Hydrogen bond	2.10
	ARG296:HN – lig:O22	Hydrogen bond	2.05
	Lig:C20 – SER293:OG	Carbon hydrogen bond	3.73
	GLU292:OE2 – lig	Pi–anion	4.41
	Lig – TRP286	Pi–pi stacked	4.30
	Lig – TRP286	Pi–pi stacked	4.61
3m	Lig:H2 – SER293:O	Hydrogen bond	2.10
	Lig:H24 – SER203:OG	Hydrogen bond	1.72
	Lig:H24 – HIS447:NE2	Hydrogen bond	2.53
	PHE295:HN – lig:O36	Hydrogen bond	2.63
	Lig:C13 – TYR124:OH	Carbon hydrogen bond	3.29
	Lig – TRP286	Pi–pi stacked	4.28
	Lig – TYR341	Pi–pi stacked	5.50
	Lig – TRP286	Pi–pi stacked	4.31
	Lig – TYR341	Pi–pi stacked	4.19
	TRP286 – lig	Pi–pi stacked	5.32
	TRP286 – lig	Pi–pi stacked	5.69
	Lig – TRP86	Pi–pi T-shaped	5.36
	TRP86 – lig	Pi–pi T-shaped	5.32

complex. π–Alkyl interaction with Val294 and the chromone ring was also observed (Fig. 9).

2.6. Molecular dynamics simulations

2.6.1 Molecular dynamics simulation studies of hCA I inhibitor. In the molecular dynamics simulation study of **3c** with hCA-I for 150 ns, C-α RMSD of hCA-I was increased from 1.0 Å to around 1.8 Å in initial 20 ns, then decreased to around 1.2 Å till 60 ns, then the gradual increase in the value was observed and the value remained around 1.6 Å while being around 1.4 Å towards the end of the simulation period (Fig. 10). During the entire simulation period of 150 ns, the C-α RMSD remained below 2.0 Å. The **3c**'s ligand's fit on protein RMSD value increased from 2.7 Å to 12.6 Å in initial 8 ns, then, after some time, gradually increased to peak 15.63 Å at around 51.75 ns, then gradually decreased to around 10.9 Å at 75.90 ns, then the sudden drop was observed to around 8 ns, and the value remained stable around 8 ns till the end of the simulation period. The **3c**'s ligand's fit on ligand RMSD remained below 1.8 Å during the simulation, and mostly showed values between 0.8 Å–1.6 Å. Protein RMSF analysis of hCA-I showed that all residues exhibited values less than 2.0 Å in fluctuations. In protein secondary structure, total SSE% % was 35.06%, where alpha-helices were 7.10% and beta-strands were 27.97%. **3c**'s Ligand RMSF analysis with hCA-I showed that the atoms of the hydroxy chromone moiety exhibited relatively higher fluctuations, with the oxygen of the hydroxy group showing values at 6.14 Å, where other atoms showed values between 3–5 Å. Protein ligand contacts revealed that Trp 5 showed the highest interaction fraction, above 1.0, and consisted mostly of water-bridges, hydrophobic, and hydrogen bonds interactions. Ligand protein contacts showed that Trp 5 maintained hydrophobic, Pi–Pi stacking with the trifluoro toluene moiety at 27%. His 64 formed polar, water-mediated interactions with nitrogen at 25%. **3c**'s torsional profile with hCA-I showed that the majority of rotatable bonds showed stable behavior during the simulation, where bonds of the trifluoromethyl moiety showed a higher dynamic profile relative to the other bonds in the compound.

In trajectory analysis, it was observed that **3c** changed its position, conformation, and orientation during the simulation; however, after around 80 ns mark, it seemed to have attained a stable pose with the hCA-I and relatively maintained the pose till the end of the simulation period. Moreover, the trifluoro toluene moiety showed relatively higher movement during the simulation as compared to the rest of the regions of **3c**.

2.6.2 Molecular dynamics simulation studies of hCA II inhibitor. In the molecular dynamics simulation study of **3c** with hCA-II for 300 ns, the C-α RMSD value increased gradually from 1.2 Å to 2.4 Å in initial 35 ns, then remained relatively stable around 2.4 Å till 177 ns mark, then multiple transient spikes around 3.2 Å were observed for next 60 ns (till 237 ns mark), despite that, the value remained mostly around 2.4 Å during the simulation, and was around 2.7 Å in the end of the simulation (Fig. 11). **3c**'s ligand fit on protein RMSD value increased to around 8.5 Å rapidly in the beginning of the simulation, and then showed a dynamic trend, where the value
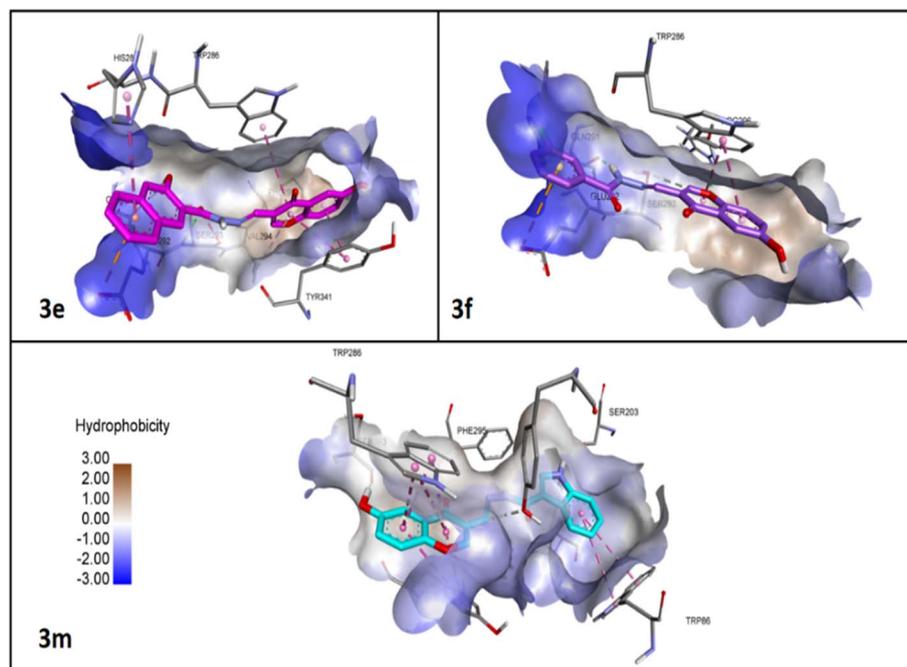
Fig. 9 Binding interactions of docked conformations of AChE inhibitors with surface representation.

remained fluctuating between around 2.6 Å to 9 Å in initial 100 ns of the simulation, then gradual increase in RMSD was observed to around 10 Å till 126 ns mark, then the value remained between 6.0 Å to 10 Å till 220 ns mark, then a gradual decrease in the value was observed, where towards the end of the simulation, **3c**'s RMSD value was around 6.8 Å. **3c**'s ligand fit on ligand RMSD value remained less than 1.1 Å during the whole simulation of 300 ns. In hCA-II's protein RMSF analysis, it was revealed that the majority of the residues showed fluctuations less than 3.0 Å, except some residues in the *N*-terminal region of the protein, which showed values up to 3.88 Å. In protein secondary structure, the total SSE% % was 35.36%, where alpha-helices were 6.68% and beta-strands were 28.68%. **3c**'s ligand RMSF analysis with hCA-II showed that the majority of atoms showed fluctuations less than 2.5 Å, where the atoms of the trifluoro toluene moiety showed relatively higher values, between 2.5 Å–3.5 Å. Protein ligand contacts showed that His 94 maintained the highest interaction during the simulation, above 2.0 interaction fraction, and consisted mostly of water-bridges, ionic, and hydrophobic interactions. Ligand protein contacts showed that the hydroxy group of the hydroxy chromone moiety maintained 100% interaction with the central zinc metal ion of the hCA-II, where His 94 maintained Pi–Pi and Pi–cation with the same moiety at around 59%, and 63%, respectively. Pro 201 maintained water-mediated hydrophobic interaction with the nitrogen at 36%. **3c**'s ligand torsion profile revealed that most rotatable bonds in the compound exhibited stable behavior during the simulation, however, bonds of the trifluoro toluene moiety showed relatively higher and dynamic torsional profiles.

In trajectory analysis, it was observed that **3c** remained attached in the active site of hCA-II and maintained the

interaction with the central zinc metal ion during the whole 300 ns simulation period. However, similar to the **3c**-hCA-I complex, most movement was observed in the trifluoromethyl moiety of the compound.

2.6.3 Molecular dynamics simulation studies of AChE inhibitor. In the molecular dynamics simulation study of **3e** with AChE for 150 ns, the C-α RMSD value increased from 1.2 Å to 2.2 Å in the initial 12 ns, then the value remained stable around 2.1 Å till the end of the simulation period of 150 ns (Fig. 12). **3e**'s ligand fit on protein RMSD increased from 1.33 Å to 8.4 Å in the initial 13 ns, then decreased gradually to around 7 Å till 19 ns, then similarly, the value remained stable around 7 Å till the end of the simulation period. **3e**'s ligand fit on ligand RMSD increased from 0.5 Å to around 1.75 Å in the initial 11 ns, then remained stable around 1.75 Å till the end of the simulation. AChE's protein RMSF analysis showed that the majority of residues exhibited values of fluctuations less than 2.7 Å, where some residues exhibited higher values, including Pro 259, Leu 386, and Asp 494 showed values at 3.52 Å, 3.49 Å, and 4.67 Å, respectively. In protein secondary structure, total SSE% % was 42.56%, where alpha-helices were 27.44% and beta-strands were 15.12%. **3e**'s ligand RMSF revealed all atoms showed fluctuations less than 2.3 Å, where most atoms showed values around 1.0 Å. Protein ligand contacts showed that Phe 295 showed the highest interaction fraction of around 1.2, and consisted mostly of water-bridges and hydrogen bonds. Ligand protein contacts showed that Phe 295 showed hydrophobic interactions with nitrogen and carbonyl group at 46% and 80% respectively. Ser 125 showed polar interaction with the hydroxy group of the hydroxy chromone moiety at around 86%. Tyr 72 and Asn 87 also showed hydrophobic and polar interactions with the same hydroxy group at 61% and 60%, respectively. **3e**'s
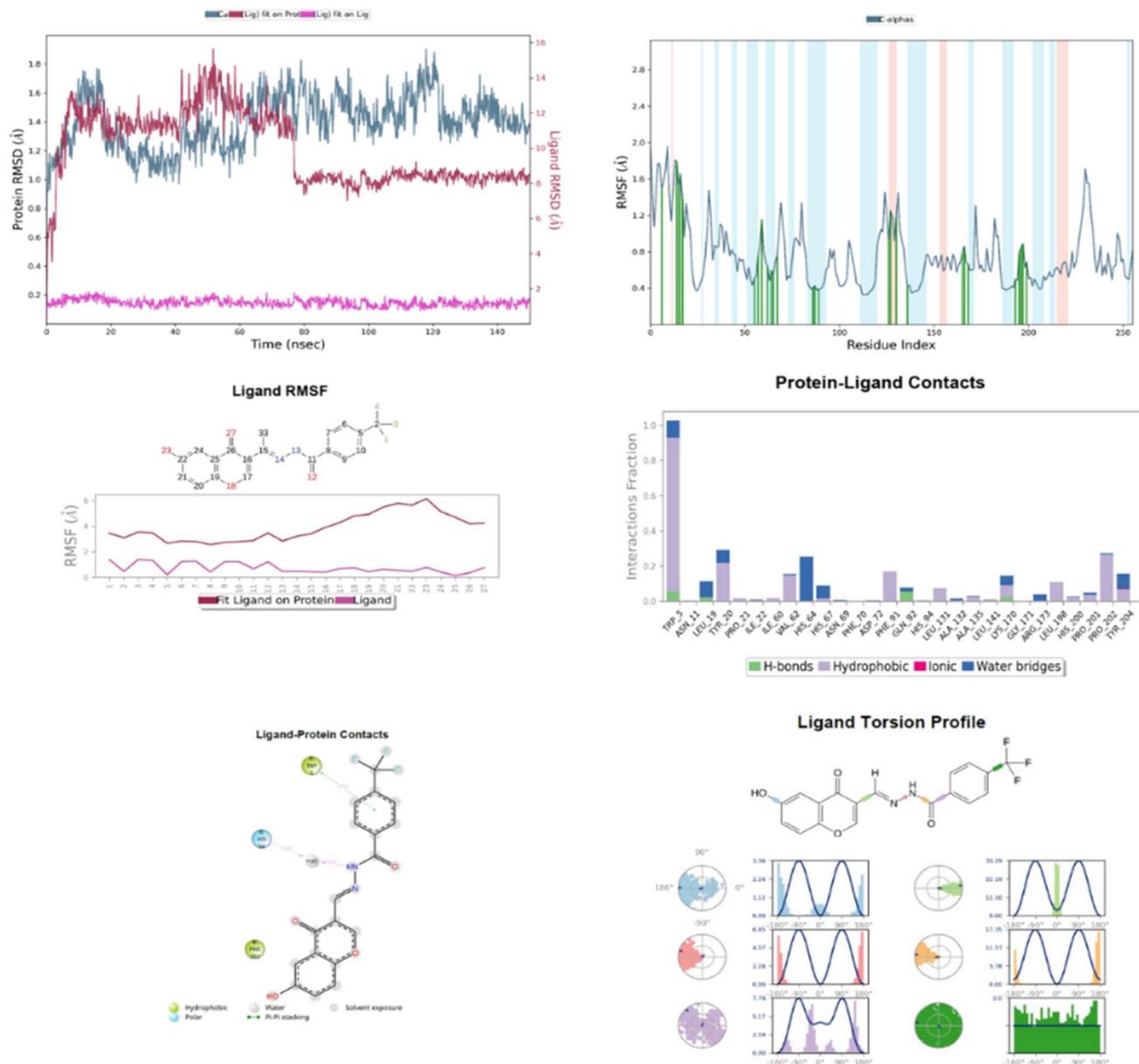
Fig. 10 MD simulation studies of complex of **3c** with hCA 1 for 150 ns; (from top left to right) RMSD plot; protein RMSF graph; ligand RMSF graph, protein ligand contacts, ligand protein contacts, and ligand torsion profile.

ligand torsion profile showed that all bonds exhibited relatively stable torsion behavior.

In trajectory analysis, it was observed that the orientation, position, and conformation of the ligand **3e** were relatively maintained, and the complex showed stable behavior during the whole simulation.

2.7. *In silico* ADME prediction

The drug-likeness of the compounds was evaluated by using Swiss ADME. All compounds showed favorable physiochemical chemical properties, such as molecular weights less than 500, good molecular flexibility as indicated by 4–5 number of rotatable bonds, favorable log P values, number of hydrogen bond acceptors and donors was also within the ideal range (<10 and

<5 respectively). The topological polar surface (TPSA) was <140, indicating favorable oral bioavailbility, which is reinforced by all compounds having high GI absorption and non-permeant to blood–brain barrier (BBB). Only **3c** was predicted to have moderate solubility, while all others had poor solubility indicating non-suitability of oral formulations (Table 6).

None of the compounds was predicted to act as a substrate of P-gp (an efflux transporter protein), therefore they have low chances of being "thrown-out" (effluxed) from the cell, increasing the efficacy of the drug molecule. Cytochrome P450 enzymes are the major detoxification enzymes, inhibition of these enzymes may result in adverse, inadvertent interactions and may interfere with metabolism of other drugs (drug–drug interactions). All compounds were predicted to inhibit CYP2C9,
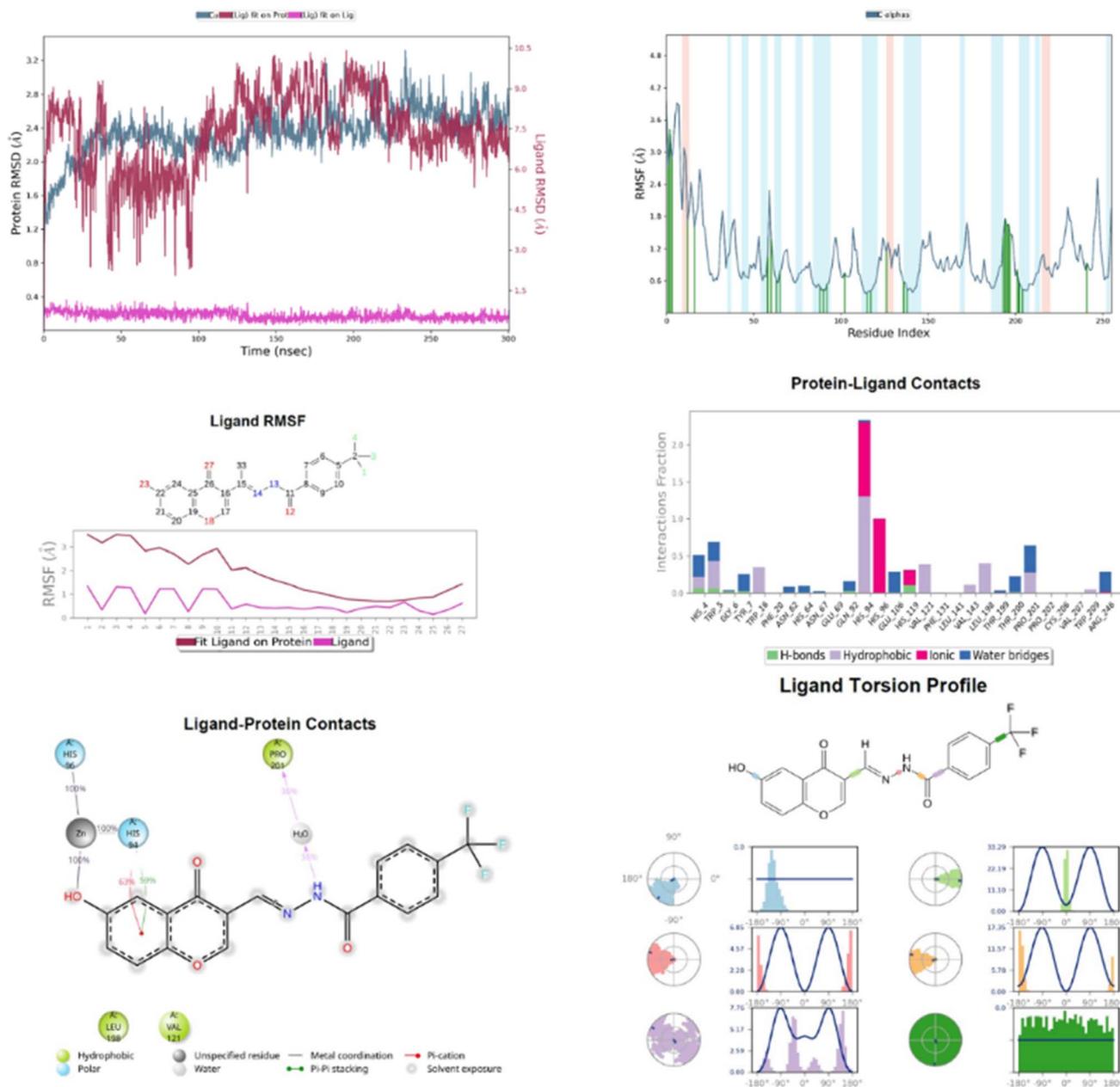
Fig. 11 MD simulation studies of complex of **3c** with hCA 2 for 150 ns; (from top left to right) RMSD plot; protein RMSF graph; ligand RMSF graph, protein ligand contacts, ligand protein contacts, and ligand torsion profile.

while all except 3e and 3h inhibited CYP1A2, whereas CYP2D6 was only inhibited with **3n** and **3m**.

2.8. Density functional theory (DFT) studies

2.8.1 Geometry optimization and frontier molecular orbitals. The optimized geometries and frontier molecular orbitals (FMO) of the six selected chromone–hydrazone derivatives **3c**, **3e**, **3f**, **3h**, **3m**, and **3n** were calculated using the DFT/B3LYP method with the 6-311G basis set. As illustrated in Fig. 13 and summarized in Table 6, all compounds exhibited negative HOMO and LUMO energy values, confirming their thermodynamic stability and suitability for participating in electronic interactions and charge-transfer processes.

The frontier orbital energy data shown in Table 7 indicate that the selected chromone–hydrazone derivatives have different HOMO, LUMO and ΔE profiles, which represent their electronic features and reactivity. The highest HOMO energies are of compounds **3n** (-0.21656 eV) and **3m** (-0.21972 eV), implying the best electron-donating capacity. On the contrary, the H value of **3h** (-0.24050 eV) is the lowest, thus it has the least nucleophilic character. In terms of LUMO energies, **3h** (-0.12599 eV) and **3f** (-0.08061 eV) show the strongest electron-accepting potential, while **3m** and **3n** have comparatively higher LUMO levels. The HOMO–LUMO energy gap, in addition, is the main criterion for which the reactivity of the compounds is distinguished. The compound **3h** has the least ΔE value (0.1145

Fig. 12 MD simulation studies of complex of **3c** with AChE for 150 ns; (from top left to right) RMSD plot; protein RMSF graph; ligand RMSF graph, protein ligand contacts, ligand protein contacts, and ligand torsion profile.

eV) indicating high charge-transfer efficiency and molecular reactivity, while the compound **3f** has the greatest energy gap (0.1545 eV) which is equivalent to high electronic stability. Moreover, the small range of ΔE_s common to all compounds can be considered an indication of biological activity potential and reactivity balance.

2.8.2 Molecular electrostatic potential. Molecular electrostatic potential (MEP) maps show distribution of electron density in a molecule and also point out parts that are likely to be attacked by electrophiles or nucleophiles. The red parts of the map denote the negative potential which is normally connected to atoms with a high electronegativity such as oxygen

and this area represents nucleophilic sites. On the other hand, the blue areas of the map show the positive potential which is frequently found next to hydrogen atoms and the spots corresponding to the electrophilic centers becoming available for nucleophilic interaction are also marked.

The chromone–hydrazone derivatives as shown in Fig. 14, have molecular surfaces with a rainbow-type electrostatic distribution. The strongest nucleophilic character and the presence of electron-rich areas are indicated by the dominance of the deep red regions, which mean highly negative electrostatic potential. Blue regions, which are the most positive potential and represent electrophilic sites, are rare and only

Table 6 Predicted *in silico* ADME properties of active inhibitors

Code	3c	3e	3n	3h	3f	3m
MW	376.29	374.35	347.32	353.29	342.73	347.32
#Rotatable bonds	5	4	4	5	4	4
#H-bond acceptors	8	6	5	7	5	5
#H-bond donors	2	3	3	2	2	3
TPSA	91.9	112.13	107.69	137.72	91.9	107.69
Consensus log P	3.18	2.74	2.29	1.57	2.61	2.29
Solubility (silicos-IT class)	Poorly soluble	Poorly soluble	Poorly soluble	Moderately soluble	Poorly soluble	Poorly soluble
GI absorption	High	High	High	High	High	High
BBB permeant	No	No	No	No	No	No
Pgp substrate	No	No	No	No	No	No
CYP1A2 inhibitor	Yes	No	Yes	No	Yes	Yes
CYP2C19 inhibitor	No	No	No	No	No	No
CYP2C9 inhibitor	Yes	Yes	Yes	Yes	Yes	Yes
CYP2D6 inhibitor	No	No	Yes	No	No	Yes
CYP3A4 inhibitor	No	No	No	No	No	No

found in limited, small areas. Transitional zones of yellow–green, which are intermediate, signify the surfaces that are polarizied to a medium degree and thus link the nucleophilic and electrophilic areas.

Electrostatic potential (ESP) analysis demonstrated significant variations in the charge distribution of selected chromone–hydrazone derivatives that may affect molecular interactions with biological targets. Table 8 shows that compounds **3e**, **3m**,

Table 7 HOMO–LUMO energies of selected compounds

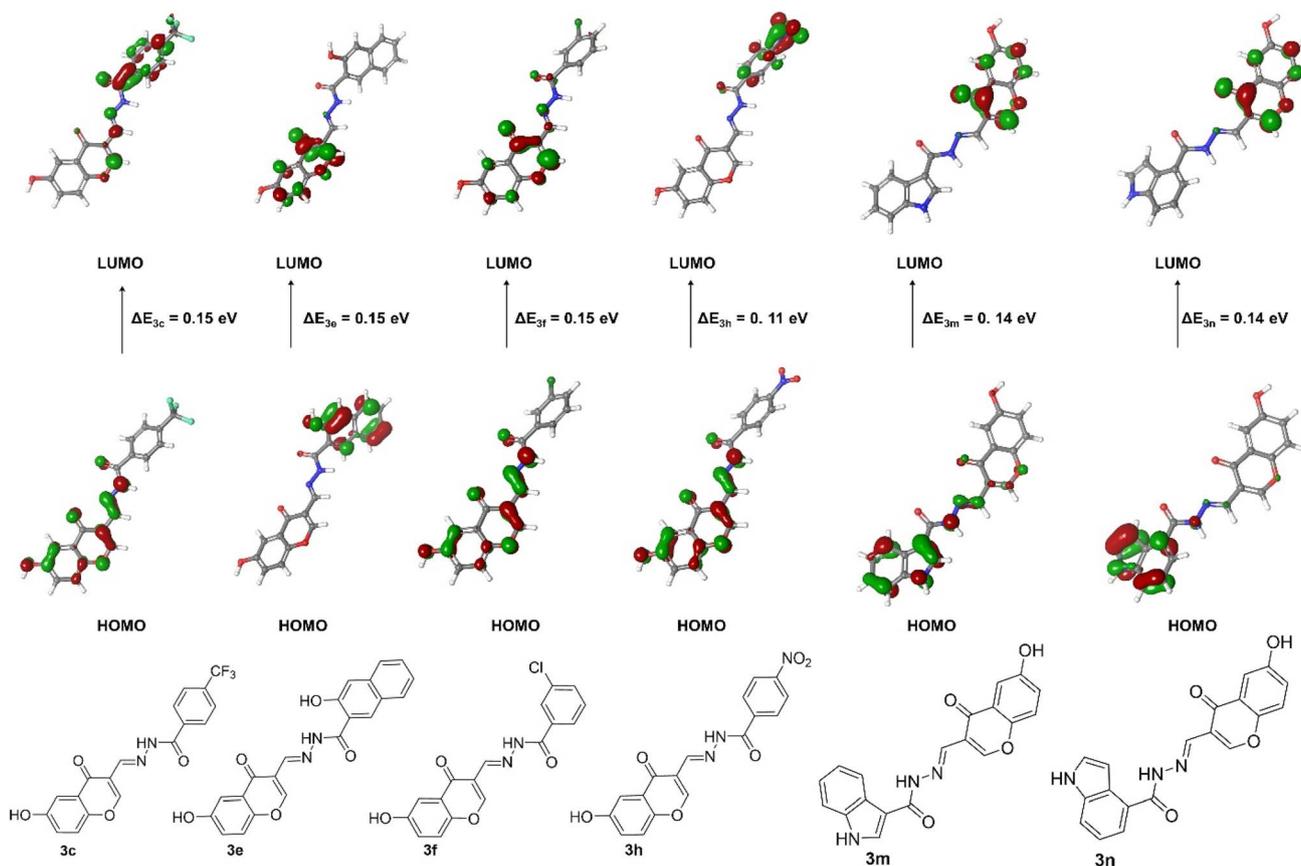| Compounds	HOMO (eV)	LUMO (eV)	ΔE (eV)
3c	−0.23804	−0.08697	0.151073
3e	−0.22600	−0.07472	0.151288
3f	−0.23511	−0.08061	0.154506
3h	−0.24050	−0.12599	0.114512
3m	−0.21972	−0.07326	0.146458
3n	−0.21656	−0.07307	0.143494

Fig. 13 HOMO–LUMO energy gap of selected compounds.
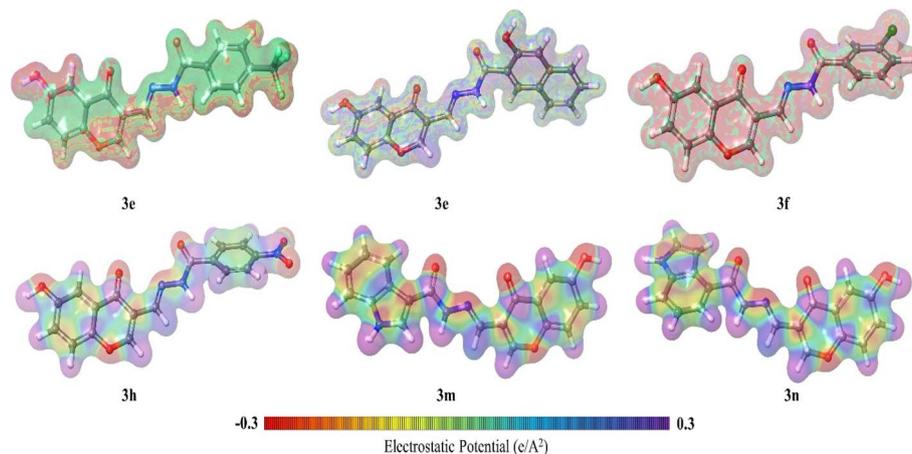
Fig. 14 Molecular electrostatic potential for selected compounds.

Table 8 Electrostatic potential for selected compounds

Compounds	ESP neg variance (eV^2)	ESP pos variance (eV^2)
3c	0.518	0.309
3e	0.688	0.264
3f	0.585	0.304
3h	0.523	0.311
3m	0.611	0.343
3n	0.630	0.269

Table 9 GCR descriptors of selected compounds^a

Compound	ΔE (eV)	μ (eV)	η (eV)	S (eV^{-1})	χ (eV)	ω (eV)
3c	0.15107	−0.16251	0.07554	6.619	0.16251	0.175
3e	0.15129	−0.15036	0.07564	6.609	0.15036	0.150
3f	0.15451	−0.15786	0.07725	6.472	0.15786	0.161
3h	0.11451	−0.18325	0.05726	8.738	0.18325	0.293
3m	0.14646	−0.14649	0.07323	6.826	0.14649	0.147
3n	0.14349	−0.14482	0.07175	6.972	0.14482	0.146

^{a} GCR descriptors: energy gap (ΔE) = E_{LUMO} − E_{HOMO}; chemical potential (μ) = (E_{HOMO} + E_{LUMO})/2; global hardness (η) = (E_{LUMO} − E_{HOMO})/2; global softness (S) = 1/2 η; electronegativity (χ) = −1/2 (E_{HOMO} + E_{LUMO}); global electrophilicity index (ω) = $\mu^2/2\eta$.

and **3n** displayed higher degrees of negative ESP variance at 0.688, 0.611, and 0.630 eV^2, respectively, marking pronounced nucleophilic regions, which could play a vital role in interactions with electrophilic centers of enzymes. On the other hand, the large variation in positive ESP, which is due to electrophilic regions, amounts to the lowest figures for these materials, with a range from 0.264 to 0.343 eV^2, but still suggests very restricted sites for nucleophilic attack. The immediate determinants of this number-value refer to the present direction of nucleophilicity in the molecule, with a well-oriented candidate for forming solid interaction with electrophilic sites of the biological target, just as the inhibition science had kept in mind for undertaking.

2.8.3 GCR (global chemical reactivity) descriptors. Global chemical reactivity (GCR) descriptors including electronegativity (χ), chemical potential (μ), hardness (η), softness (S), and electrophilocity (ω) are valuable tools to forecast reactivity, stability, and biologically active potential of a molecule as well. They help in anticipating enzyme–receptor interaction and helping in the designing of drugs. These GCR described specific chromone–hydrazone derivatives relationship shown in Table 9.

For the three cases associated with energy gap, **3h** compares weakly with **3f** in ΔE. The smaller energy gap suggests a higher chemical reactivity and the opportunity for a higher charge transfer. By deduction, the stated energy gap has revealed the outcome of **3h** interacting quite well with target molecular mechanisms.

Negative chemical potential (μ) values have been calculated for all compounds due to the electron-donating tendencies of molecules, with **3h** having the most negative value (−0.18325 eV) as being prone to electron distribution. Global hardness η follows the same trend, in which **3h** is the lowest value (0.05726 eV), thus indicating it is more reactive; **3f** is highest with hardness (0.07725 eV), representing more electronic stability. Global softness (S), the inverse of hardness, highlights **3h** as the softest compound (8.738 eV^{-1}), consistent with its higher reactivity. The electronegativity (χ) values mirror the chemical potential, with **3h** being the most electronegative (0.18325 eV), and the electrophilicity index (ω) is highest for **3h** (0.293 eV), indicating its strong capability to accept electrons in interactions with nucleophilic centers. According to GCR analysis, **3h** is the most chemically reactive and electrophilic derivative among the series; however, **3f**, **3m**, and **3n** are relatively stable and less reactive.

3 Conclusion

In summary, a detail study entails the development of novel hydrazone substituted chromone derivatives (**3a–p**) and evaluating their therapeutic potential as multi-target medicinal compounds. In a comprehensive screening activity, most of

them fully inhibit the enzyme acetylcholinesterase (AChE). Some of the most active compounds are **3e** (IC_{50} = 0.20 μM), **3c** (IC_{50} = 0.82 μM), and **3f** (IC_{50} = 1.11 μM), and structural features such as trifluoromethyl phenyl and hydroxy naphthol groups appear to explain their activity profiles. Meanwhile, all the discovered compounds exhibited significant inhibition of human hCA I and hCA II, with compounds **3c**, **3e**, and **3n** exhibiting considerable activity (IC_{50} values roughly around 3–5 μM). Molecular docking and dynamics simulation inferences were drawn on the mode of binding within the active sites of these enzymes, with indications emphasizing on the key interactions of zinc coordination, hydrogen bonding with conserved sites such as Gln92, and hydrophobic interactions with amino acids like Val121, Leu198, and Val143. The ABTS and DPPH evaluations evaluating the generation of antioxidants have been found to be very good radical species scavengers, in particular for compounds **3c**, **3e**, and **3m**, indicating their potential against oxidative stress. The structure–activity relationship analysis (SARs) observed with respect to the different substituents namely hydroxynaphthol and trifluoro-methyl groups that enhance enzyme inhibition and antioxidant activities and nitrate or chlorophenyl and pyridinyl groups destroy the potency of the proposed compounds. Altogether, the outcomes emphasize the hope of these chromone hydrazones as drugs with a variety of functions that are able to cure neurodegenerative and metabolic diseases, in particular, Alzheimer's, by enzyme inhibition and antioxidant mechanisms. The computational findings confirm that the derivatives possess balanced electronic stability and reactivity profiles, consistent with their potential to form favorable interactions with biological targets. Knowledge about their molecular structure as well as the way they behave biologically could also be of great assistance by means of the contribution of these novel chemical substances to the pharma industry as possible drug candidates.

4   Material and methods

4.1.   Chemistry

All the chemicals were purchased from Fluka Chemie AG Buchs and Sigma-Aldrich and used without further purification. Reactions were monitored by thin-layer chromatography (TLC) on silica gel 60 F254 aluminum sheets. The mobile phase was ethyl acetate: petroleum ether (1:1) and detection was made using UV light. ^{1}H NMR and ^{13}C NMR spectra were registered in DMSO on Bruker NMR instrument with Topspin software (400 MHz). HRMS data were acquired *via* Thermo Fisher Scientific Q Exactive™ Hybrid Quadrupole-Orbitrap™ instrument.

4.1.1   Preparation of chromone hydrazone 3(a–p)

4.1.1.1 General procedure. The synthesis of hydrazide derivatized chromones is carried out by the method reported in literature.[55] According to given approach, alcoholic solution of 8-hydroxy chromone (1 mmol) was treated with differently substituted hydrazide using 2 to 3 drops of glacial acetic acid as a catalyst. The reaction mixture was refluxed at 65–70 °C for three hours and reaction progress is carefully monitored by TLC (hexane/ethyl acetate: 7/3). Upon completion, the mixture is precipitated by pouring into ice cold water and the product (**3a–**

p) was filtered, washed with MeOH and dried in oven for further studies Fig. 1. The synthesized compounds are well characterized by ^{1}HNMR and ^{13}CNMR.

4.1.2   (E)-2-Chloro-N′-((6-hydroxy-4-oxo-4H-chromen-3-yl)methylene)benzohydrazide 3a.
White solid, yield: 82%, mp: 237–239 °C. ^{1}H NMR (400 MHz, DMSO-d_6) δ 11.98 (s, 1H), 10.14 (s, 1H), 8.80 (s, 1H), 8.45 (s, 1H), 7.70–7.53 (m, 3H), 7.50–7.43 (m, 2H), 7.39 (d, J = 3.0 Hz, 1H), 7.26 (ddd, J = 18.9, 9.1, 3.0 Hz, 1H). ^{13}C NMR (101 MHz, DMSO-d_6) δ 175.23, 162.83, 155.83, 154.91, 150.00, 141.56, 135.60, 131.92, 130.89, 130.24, 129.78, 127.76, 124.75, 124.00, 120.58, 117.50, 108.22. HPLC-PDA: λ 254 nm, MeCN:MeOH (1:1), Rt: 4.42 min, 99.29%. HRMS-ESI (m/z): chemical formula: $C_{17}H_{11}ClN_2O_4$, calculated [M + H]$^+$: 342.0407, found: 341.0335.

4.1.3   (E)-N′-((6-hydroxy-4-oxo-4H-chromen-3-yl)methylene)-2-methylbenzohydrazide 3b.
White solid, yield: 88%, mp: 232–234 °C. ^{1}H NMR (400 MHz, DMSO-d_6) δ 11.82 (s, 1H), 10.13 (s, 1H), 8.78 (s, 1H), 8.47 (s, 1H), 7.60 (d, J = 9.0 Hz, 1H), 7.46 (d, J = 7.4 Hz, 1H), 7.40 (dd, J = 6.4, 2.2 Hz, 1H), 7.37–7.20 (m, 3H), 2.39 (s, 3H). ^{13}C NMR (101 MHz, DMSO-d_6) δ 175.26, 165.57, 155.80, 154.67, 150.00, 140.82, 136.37, 135.64, 131.09, 130.42, 127.91, 126.12, 124.75, 123.96, 120.56, 117.70, 108.21, 19.76. HPLC-PDA: λ 254 nm, MeCN:MeOH (1:1), Rt: 4.39 min, 98.92%. HRMS-ESI (m/z): chemical formula: $C_{18}H_{14}N_2O_4$, calculated [M + H]$^+$: 322.0953, found: 323.1021.

4.1.4   (E)-N′-((6-hydroxy-4-oxo-4H-chromen-3-yl)methylene)-4-(trifluoromethyl)benzohydrazide 3c.
White solid, yield: 74%, mp: 223–225 °C. ^{1}H NMR (400 MHz, DMSO-d_6) δ 12.11 (s, 1H), 10.15 (s, 1H), 8.80 (s, 1H), 8.66 (s, 1H), 8.14 (d, J = 8.0 Hz, 2H), 7.92 (d, J = 8.0 Hz, 2H), 7.60 (d, J = 9.0 Hz, 1H), 7.40 (d, J = 3.0 Hz, 1H), 7.29 (dd, J = 9.0, 3.0 Hz, 1H). ^{13}C NMR (101 MHz, DMSO-d_6) δ 175.29, 162.23, 155.84, 154.80, 150.00, 142.09, 137.50, 132.23, 129.04, 125.95, 125.91, 124.75, 123.98, 120.55, 117.56, 108.23. HPLC-PDA: λ 254 nm, MeCN:MeOH (1:1), Rt: 4.39 min, 98.94%. HRMS-ESI (m/z): chemical formula: $C_{18}H_{11}F_3N_2O_4$, calculated [M + H]$^+$: 376.0670, found: 377.0749.

4.1.5   (E)-N′-((6-hydroxy-4-oxo-4H-chromen-3-yl)methylene)-2-(1H-pyrrolo[2,3-b]pyridin-1-yl)acetohydrazide 3d.
Light yellow solid, yield: 78%, mp: 269–270 °C. ^{1}H NMR (400 MHz, DMSO-d_6) δ 11.68 (s, 1H), 10.14 (s, 1H), 8.89 (s, 1H), 8.32–8.12 (m, 2H), 7.98 (dd, J = 7.8, 1.7 Hz, 1H), 7.60 (d, J = 9.1 Hz, 1H), 7.56 (dd, J = 5.6, 3.5 Hz, 1H), 7.41 (d, J = 3.0 Hz, 1H), 7.28 (dd, J = 9.0, 3.1 Hz, 1H), 7.14–7.04 (m, 1H), 5.49 (s, 2H). ^{13}C NMR (101 MHz, DMSO-d_6) δ 175.15, 169.62, 155.80, 154.83, 150.01, 148.07, 142.60, 137.12, 131.03, 128.83, 124.78, 123.95, 120.57, 120.50, 117.62, 116.12, 108.22, 99.56, 45.68. HPLC-PDA: λ 254 nm, MeCN:MeOH (1:1), Rt: 4.12 min, 99.78%. HRMS-ESI (m/z): chemical formula: $C_{19}H_{14}N_4O_4$, calculated [M + H]$^+$: 362.1015, found: 363.1081.

4.1.6   (E)-3-Hydroxy-N′-((6-hydroxy-4-oxo-4H-chromen-3-yl)methylene)-2-naphthohydrazide 3e.
White solid, yield: 83%, mp: 253–255 °C. ^{1}H NMR (400 MHz, DMSO-d_6) δ 12.08 (s, 1H), 11.30 (s, 1H), 10.16 (s, 1H), 8.82 (s, 1H), 8.63 (s, 1H), 8.46 (s, 1H), 7.91 (d, J = 8.2 Hz, 1H), 7.77 (d, J = 8.3 Hz, 1H), 7.61 (d, J = 9.0 Hz, 1H), 7.58–7.44 (m, 1H), 7.41 (d, J = 3.0 Hz, 1H), 7.37 (s, 0H), 7.33 (s, 1H), 7.30 (dd, J = 9.0, 3.0 Hz, 1H). ^{13}C NMR (101 MHz, DMSO-d_6) δ 175.29, 164.56, 155.85, 154.91, 154.83, 150.01,

142.04, 136.37, 130.46, 129.10, 128.72, 127.21, 126.33, 124.77, 124.26, 124.00, 120.58, 120.47, 117.59, 111.07, 108.24. HPLC-PDA: λ 254 nm, MeCN : MeOH (1 : 1), Rt: 4.51 min, 95.81%. HRMS-ESI (m/z): chemical formula: $C_{21}H_{14}N_2O_5$, calculated [M + H]$^+$: 374.0902, found: 375.0969 (397.0789 [M + Na]$^+$).

4.1.7 (E)-3-Chloro-N'-((6-hydroxy-4-oxo-4H-chromen-3-yl) methylene)benzohydrazide 3f.
White solid, yield: 84%, mp: 226–228 °C. ^{1}H NMR (400 MHz, DMSO-d_6) δ 12.00 (s, 1H), 10.15 (s, 1H), 8.78 (s, 1H), 8.64 (s, 1H), 7.99 (t, J = 1.9 Hz, 1H), 7.91 (d, J = 7.8 Hz, 1H), 7.71–7.64 (m, 1H), 7.63–7.53 (m, 2H), 7.40 (d, J = 3.0 Hz, 1H), 7.29 (dd, J = 9.0, 3.0 Hz, 1H). ^{13}C NMR (101 MHz, DMSO-d_6) δ 175.30, 161.94, 155.82, 154.74, 149.99, 141.81, 135.67, 133.79, 132.09, 130.96, 127.82, 126.93, 124.75, 123.97, 120.55, 117.59, 108.24. HPLC-PDA: λ 254 nm, MeCN : MeOH (1 : 1), Rt: 4.27 min, 99.79%. HRMS-ESI (m/z): chemical formula: $C_{17}H_{11}ClN_2O_4$, calculated [M − H]$^+$: 342.0407, found: 341.0334.

4.1.8 (E)-N'-((6-hydroxy-4-oxo-4H-chromen-3-yl) methylene)-4-methoxybenzohydrazide 3g.
White solid, yield: 79%, mp: 240–242 °C. ^{1}H NMR (400 MHz, DMSO-d_6) δ 11.80 (s, 1H), 10.14 (s, 1H), 8.75 (s, 1H), 8.63 (s, 1H), 7.94 (d, J = 8.4 Hz, 2H), 7.59 (d, J = 9.0 Hz, 1H), 7.40 (d, J = 3.0 Hz, 1H), 7.29 (dd, J = 9.0, 3.0 Hz, 1H), 7.06 (d, J = 8.4 Hz, 2H), 3.85 (s, 3H). ^{13}C NMR (101 MHz, DMSO-d_6) δ 175.35, 162.85, 162.53, 155.78, 154.43, 150.01, 140.48, 130.04, 125.73, 124.76, 123.94, 120.54, 117.84, 114.19, 108.22, 55.90. HPLC-PDA: λ 254 nm, MeCN : MeOH (1 : 1), Rt: 4.12 min, 99.82%. HRMS-ESI (m/z): chemical formula: $C_{18}H_{14}N_2O_5$, calculated [M − H]$^+$: 338.0902, found: 337.0832.

4.1.9 (E)-N'-((6-hydroxy-4-oxo-4H-chromen-3-yl) methylene)-4-nitrobenzohydrazide 3h.
Yellow solid, yield: 85%, mp: 259–261 °C. ^{1}H NMR (400 MHz, DMSO-d_6) δ 12.18 (s, 1H), 10.15 (s, 1H), 8.80 (s, 1H), 8.65 (s, 1H), 8.37 (d, J = 8.3 Hz, 2H), 8.17 (d, J = 8.4 Hz, 2H), 7.60 (d, J = 9.0 Hz, 1H), 7.39 (d, J = 3.0 Hz, 1H), 7.28 (dd, J = 9.0, 3.0 Hz, 1H). ^{13}C NMR (101 MHz, DMSO-d_6) δ 175.27, 161.72, 155.84, 154.89, 149.99, 149.77, 142.43, 139.33, 129.64, 124.75, 124.09, 124.00, 120.57, 117.48, 108.23. HPLC-PDA: λ 254 nm, MeCN : MeOH (1 : 1), Rt: 4.02 min, 100%. HRMS-ESI (m/z): chemical formula: $C_{17}H_{11}N_3O_6$, calculated [M − H]$^+$: 353.0647, found: 352.0580.

4.1.10 (E)-N'-((6-hydroxy-4-oxo-4H-chromen-3-yl) methylene)isonicotinohydrazide 3i.
White solid, yield: 75%, mp: 252–254 °C. ^{1}H NMR (400 MHz, DMSO-d_6) δ 12.11 (s, 1H), 10.14 (d, J = 11.5 Hz, 1H), 8.83–8.76 (m, 3H), 8.64 (s, 1H), 7.83 (d, J = 5.0 Hz, 2H), 7.61 (d, J = 8.9 Hz, 1H), 7.39 (s, 1H), 7.32–7.26 (m, 1H). ^{13}CNMR (101 MHz, DMSO-d_6) δ 174.98, 160.75, 155.50, 154.51, 149.79, 149.70, 148.69, 142.39, 138.12, 127.15, 124.53, 123.64, 122.92, 120.26, 117.67, 107.96, 40.35, 40.14, 39.94, 39.73, 39.52, 39.31, 39.10. HPLC-PDA: λ 254 nm, MeCN : MeOH (1 : 1), Rt: 3.98 min, 99.66%. HRMS-ESI (m/z): chemical formula: $C_{16}H_{11}N_3O_4$, calculated [M − H]$^+$: 309.0749, found: 308.0678.

4.1.11 (E)-2-Bromo-N'-((6-hydroxy-4-oxo-4H-chromen-3-yl) methylene)benzohydrazide 3j.
White solid, yield: 80%, mp: 230–232 °C. ^{1}H NMR (400 MHz, DMSO-d_6) δ 11.96 (s, 1H), 10.14 (s, 1H), 8.80 (s, 1H), 8.44 (s, 1H), 7.73 (dd, J = 8.0, 1.2 Hz, 1H), 7.61 (d, J = 9.0 Hz, 1H), 7.55 (d, J = 1.9 Hz, 1H), 7.50–7.41 (m, 2H), 7.39 (d, J = 3.0 Hz, 1H), 7.29 (dd, J = 9.1, 3.0 Hz, 1H). ^{13}C NMR (101 MHz, DMSO-d_6) δ 175.22, 163.67, 155.83, 154.90, 150.00, 141.53, 137.75, 133.33, 132.02, 129.75, 128.22, 124.74,

124.00, 120.59, 119.89, 117.49, 108.22. HPLC-PDA: λ 254 nm, MeCN : MeOH (1 : 1), Rt: 3.95 min, 99.28%. HRMS-ESI (m/z): chemical formula: $C_{17}H_{11}BrN_2O_4$, calculated [M − H]$^+$: 385.9902/387.9882, found: 384.9831/386.9812.

4.1.12 (E)-4-Bromo-N'-((6-hydroxy-4-oxo-4H-chromen-3-yl) methylene)benzohydrazide 3k.
Light yellow solid, yield: 80%, mp: 237–239 °C. ^{1}H NMR (400 MHz, DMSO-d_6) δ 11.98 (s, 1H), 10.14 (s, 1H), 8.78 (s, 1H), 8.63 (s, 1H), 7.89 (d, J = 8.2 Hz, 2H), 7.75 (d, J = 8.1 Hz, 2H), 7.60 (d, J = 9.0 Hz, 1H), 7.39 (d, J = 3.0 Hz, 1H), 7.28 (dd, J = 9.0, 3.0 Hz, 1H). ^{13}C NMR (101 MHz, DMSO-d_6) δ 175.30, 162.46, 155.81, 154.69, 150.00, 141.57, 132.76, 131.99, 130.20, 126.07, 124.75, 123.98, 120.56, 117.63, 108.22, 49.08. HPLC-PDA: λ 254 nm, MeCN : MeOH (1 : 1), Rt: 3.92 min, 99.91%. HRMS-ESI (m/z): chemical formula: $C_{17}H_{11}BrN_2O_4$, calculated [M + Na]$^+$: 407.9722/409.9701, found: 408.9791/410.9772.

4.1.13 (E)-N'-((6-hydroxy-4-oxo-4H-chromen-3-yl) methylene)-2-phenylacetohydrazide 3l.
White solid, yield: 81%, mp: 241–243 °C. ^{1}H NMR (400 MHz, DMSO-d_6) δ 11.67 (s, 1H), 11.40 (s, 1H), 10.12 (d, J = 4.7 Hz, 2H), 8.79 (s, 1H), 8.68 (s, 1H), 8.38 (s, 1H), 8.14 (s, 1H), 7.58 (dd, J = 9.0, 4.8 Hz, 2H), 7.41–7.18 (m, 17H), 3.53 (s, 2H). ^{13}C NMR (101 MHz, DMSO-d_6) δ 175.28, 172.70, 166.86, 155.75, 154.50, 149.98, 139.92, 136.23, 136.08, 129.96, 129.52, 128.66, 127.07, 126.81, 124.75, 123.91, 120.53, 117.79, 108.20, 41.71. HPLC-PDA: λ 254 nm, MeCN : MeOH (1 : 1), Rt: 4.34 min, 99.82%. HRMS-ESI (m/z): chemical formula: $C_{18}H_{14}N_2O_4$, calculated [M − H]$^+$: 322.0953, found: 321.0881.

4.1.14 (E)-N'-((6-hydroxy-4-oxo-4H-chromen-3-yl) methylene)-1H-indole-3-carbohydrazide 3m.
White solid, yield: 83%, mp: 259–261 °C. ^{1}H NMR (400 MHz, DMSO-d_6) δ 11.74 (d, J = 3.1 Hz, 1H), 11.46 (s, 1H), 10.13 (s, 1H), 8.77 (s, 1H), 8.64–7.84 (m, 4H), 7.60 (d, J = 9.0 Hz, 1H), 7.49 (d, J = 7.6 Hz, 1H), 7.42 (d, J = 3.0 Hz, 1H), 7.29 (dd, J = 9.0, 3.0 Hz, 1H), 7.24–7.09 (m, 2H). ^{13}C NMR (101 MHz, DMSO-d_6) δ 175.76, 174.17, 160.09, 158.46, 156.04, 152.26, 140.50, 134.93, 129.98, 128.01, 127.91, 124.58, 124.54, 122.78, 122.61, 121.71, 120.56, 117.49, 109.76. HPLC-PDA: λ 254 nm, MeCN : MeOH (1 : 1), Rt: 4.03 min, 99.92%. HRMS-ESI (m/z): chemical formula: $C_{19}H_{13}N_3O_4$, calculated [M − H]$^+$: 347.0906, found: 346.0833.

4.1.15 (E)-N'-((6-hydroxy-4-oxo-4H-chromen-3-yl) methylene)-1H-indole-4-carbohydrazide 3n.
White solid, yield: 82%, mp: 244–246 °C. ^{1}H NMR (400 MHz, DMSO-d_6) δ 11.84 (s, 1H), 11.36 (s, 1H), 10.14 (s, 1H), 8.69 (d, J = 72.6 Hz, 2H), 7.61 (dd, J = 8.5, 6.9 Hz, 2H), 7.56–7.46 (m, 2H), 7.40 (d, J = 3.0 Hz, 1H), 7.29 (dd, J = 9.0, 3.0 Hz, 1H), 7.20 (t, J = 7.7 Hz, 1H), 6.85 (s, 1H). ^{13}C NMR (101 MHz, DMSO-d_6) δ 175.35, 155.77, 154.40, 150.02, 140.07, 137.00, 127.31, 126.80, 125.44, 124.78, 123.94, 120.62, 120.56, 119.37, 118.00, 115.28, 108.22, 102.17. HPLC-PDA: λ 254 nm, MeCN : MeOH (1 : 1), Rt: 4.04 min, 99.83%. HRMS-ESI (m/z): chemical formula: $C_{19}H_{13}N_3O_4$, calculated [M − H]$^+$: 347.0906, found: 346.0833.

4.1.16 (E)-N'-((6-hydroxy-4-oxo-4H-chromen-3-yl) methylene)furan-2-carbohydrazide 3o.
White solid, yield: 80%, mp: 250–252 °C. ^{1}H NMR (400 MHz, DMSO-d_6) δ 11.93 (s, 1H), 10.14 (s, 1H), 8.77 (s, 1H), 8.62 (s, 1H), 7.98–7.88 (m, 1H), 7.60 (d, J = 9.0 Hz, 1H), 7.40 (d, J = 3.0 Hz, 1H), 7.36–7.22 (m, 2H), 6.71 (dd, J = 3.5, 1.7 Hz, 1H). ^{13}C NMR (101 MHz, DMSO-d_6)

δ 175.25, 155.79, 154.68, 149.97, 147.51, 146.40, 141.24, 128.87, 124.76, 123.95, 120.54, 117.67, 115.41, 112.53, 108.23. HPLC-PDA: λ 254 nm, MeCN : MeOH (1 : 1), Rt: 3.91 min, 99.98%. HRMS-ESI (*m/z*): chemical formula: $C_{15}H_{10}N_2O_5$, calculated [M − H]$^+$: 298.0589, found: 297.0517.

4.1.17 (E)-N′-((6-hydroxy-4-oxo-4H-chromen-3-yl) methylene)picolinohydrazide 3p. Light yellow solid, yield: 83%, mp: 234–236 °C. ^{1}H NMR (400 MHz, DMSO-d_6) δ 12.34 (s, 1H), 10.15 (s, 1H), 8.79 (d, *J* = 8.3 Hz, 2H), 8.73 (dt, *J* = 4.5, 1.4 Hz, 1H), 8.29–8.12 (m, 1H), 8.08–7.96 (m, 1H), 7.67 (ddd, *J* = 7.5, 4.8, 1.4 Hz, 1H), 7.60 (d, *J* = 9.0 Hz, 1H), 7.41 (d, *J* = 3.0 Hz, 1H), 7.29 (dd, *J* = 9.0, 3.0 Hz, 1H). ^{13}C NMR (101 MHz, DMSO-d_6) δ 175.27, 161.03, 155.79, 154.79, 150.07, 149.99, 148.98, 142.67, 138.41, 127.44, 124.81, 123.93, 123.20, 120.54, 117.95, 108.24. HPLC-PDA: λ 254 nm, MeCN : MeOH (1 : 1), Rt: 4.03 min, 100%. HRMS-ESI (*m/z*): chemical formula: $C_{16}H_{11}N_3O_4$, calculated [M − H]$^+$: 309.0749, found: 308.0678.

4.2. Molecular dynamics simulations

In the molecular dynamics simulations using Desmond (D.E. Shaw) on Schrödinger Maestro 2024.4 program, complexes of **3c** with CA-I and CA-II, and **3e** with AChE were first treated with protein preparation workflow by options opting for replacing hydrogens, assigning bond orders using CCD database, creating zero-order bonds to metals and disulfide bonds, deleting water molecules, and filling in missing side chains if required. In the H-bonds assignment optimization, sample water orientations, considering all ligand states, and the PROPKA pH 7.4 option were used. In the system builder panel, the TIP3P solvent model was used for solvation in the orthorhombic box using buffer settings with 10 Å x 10 Å x 10 Å, and the minimized volume option was used; then ions for neutralization with 0.15 M NaCl salt were placed. The complex of **3c** with CA-I, after solvation, resulted in 26 108 atoms, **3c** with CA-II in 27 601, and **3e** with AChE in 50 100 atoms, respectively. Initially, for each complex, in the molecular dynamics panel, a 150 ns (nanoseconds) simulation time was entered. At the same time, the recording interval was set to 150 ps (picoseconds), with energy option at 1.2, resulting in an approximation for 1000 frames. For the final run, the NPT ensemble class was set at 300.0 kelvin with Nosé-Hoover chain temperature coupling and 1.01325 bar pressure with Martyna-Tobias-Klein pressure coupling. The system followed the default relaxation protocol before the simulation, which included small simulations, using NVT and NPT ensembles with different restraint parameters. For the **3c**-CAII complex, the total simulation time was extended to 300 ns, and the initial simulation of 150 ns was extended using the last frame as extension starting reference. This resulted in a total of 2004 frames of simulation for the complex. However, during extension, all simulation settings were kept the same, and the default relaxation procedure was not exercised for extension.

4.3. Density functional theory studies

The geometric structures of the investigated compounds were optimized using DFT at the B3LYP/6-311G(d,p) level. The B3LYP functional combined with the 6-311G(d,p) basis set was chosen because it provides reliable descriptions of molecular geometries, frontier molecular orbitals, and electronic distributions in organic systems. The inclusion of polarization functions allows a more accurate treatment of electron density, which is essential for evaluating structure–property relationships in the studied hydrazone derivatives. The calculations ran on Gaussian 16 and the outputs in the form of geometries were analyzed using GaussView 6.0. One way to analyze the electronic character of the molecules was to look at the frontier molecular orbitals (HOMO and LUMO). This method provides us an overview of where the electrons are distributed and possible charge-transfer paths with the potential to occur. A range of reactivity descriptors whose global aspects constituted ionization potential, electron affinity, electronegativity, chemical hardness, chemical potential, and electrophilicity index was evaluated from the corresponding frontier orbital energies, implying the reactivity, stability, and electronic interaction properties of the compounds at hand were predictable. Moreover, for the purpose of locating the regions most susceptible to electrophilic or nucleophilic attack, the Molecular Electrostatic Potential (MEP) surfaces were plotted, and these MEP surfaces were illustrated using Avogadro.

4.4. Cytotoxicity assay

Human umbilical vein endothelial cells (HUVEC, ATCC® PCS-100-010™) were used to evaluate the cytotoxic effects of the most active compounds. Cells were cultured in DMEM supplemented with 10% fetal bovine serum (FBS) and 1% penicillin/streptomycin under standard conditions (37 °C, 5% CO_2). Cytotoxicity was determined using the MTT assay. Briefly, cells were seeded into 96-well plates and treated with test compounds serially diluted in the range of 200–3.125 μM. After incubation, MTT solution was added and the formed formazan crystals were dissolved in DMSO, and absorbance was measured at 570 nm. All experiments were performed in triplicate ($n = 3$), and IC$_{50}$ values were calculated from dose–response curves and expressed as mean ± SD.

5 Limitations and future perspectives

Although the present study provides comprehensive *in vitro* enzyme inhibition, antioxidant evaluation, and computational analysis of the synthesized hydrazone derivatives, some limitations should be acknowledged. The biological activities were assessed under *in vitro* conditions, and therefore the results may not fully reflect *in vivo* behavior, including pharmacokinetics, bioavailability, and toxicity profiles. In addition, the antioxidant activity was evaluated using chemical radical-scavenging assays, which do not account for complex biological redox environments. Future studies will focus on *in vivo* validation, detailed toxicity assessments, and further mechanistic investigations, as well as structural optimization to improve selectivity and drug-like properties of the most promising compounds.

Author contributions

Wajeeha Zareen: investigation, formal analysis. Nadeem Ahmed: writing – original draft, Ayşe Merve Senol, Orhan

Ulucay, Feyzi Sinan Tokali, Parham Taslimi: investigation, validation, software, data curation, writing – original draft. Talha Islam, Mariya al-Rashida: data curation, software, validation, Zahid Shafiq: writing – original draft, supervision, conceptualization. Ahmed Mohamed Tawfeek, Mohammad Shahidul Islam: resources, investigation, funding acquisition.

Conflicts of interest

The authors declare that they have no known competing financial interests or personal relationships that could have appeared to influence the work reported in this paper.

Data availability

The data supporting this article have been included as part of the supplementary information (SI). Supplementary information: NMR (^{1}H and ^{13}C) and HRMS spectra of all the new compounds are available as supporting material. Furthermore, IC$_{50}$ graphs and K_i graphs of enzyme assay and antioxidant activity are given in SI. See DOI: https://doi.org/10.1039/d5ra10080a.

Acknowledgements

References

1 G. Ç. Turgut, F. Çakır, A. Şen, F. S. Tokalı and H. Şenol, Novel thiazolidinedione hybrids as cholinesterase inhibitors and targeting neuroblastoma: design, synthesis, *in vitro* and *in silico* biological evaluations, *Bioorg. Chem.*, 2025, 108869.

2 K. L. Lanctôt, J. Amatniek, S. Ancoli-Israel, S. E. Arnold, C. Ballard, J. Cohen-Mansfield, Z. Ismail, C. Lyketsos, D. S. Miller and E. Musiek, Neuropsychiatric signs and symptoms of Alzheimer's disease: New treatment paradigms, *Alzheimer's Dement.: Transl. Res. Clin. Interv.*, 2017, **3**(3), 440–449.

3 K. M. Fiest, J. I. Roberts, C. J. Maxwell, D. B. Hogan, E. E. Smith, A. Frolkis, A. Cohen, A. Kirk, D. Pearson and T. Pringsheim, The prevalence and incidence of dementia due to Alzheimer's disease: a systematic review and meta-analysis, *Can. J. Neurol. Sci.*, 2016, **43**(S1), S51–S82.

4 R. E. Becker, N. H. Greig and E. Giacobini, Why do so many drugs for Alzheimer's disease fail in development? Time for new methods and new practices?, *J. Alzheimers Dis.*, 2008, **15**(2), 303–325.

5 P. Arora, S. R. Swati, S. Jha, S. Gupta and S. Kumar, Innovative approaches in acetylcholinesterase inhibition: a pathway to effective Alzheimer's disease treatment, *Mol. Divers.*, 2025, 1–30.

6 Y. Demir, H. Şenol, O. Uluçay, Ş. Ateşoğlu and F. S. Tokalı, Morpholine-Modified Thiosemicarbazones and Thiazolidin-4-ones against Alzheimer's Key Enzymes: From Synthesis to Inhibition, *Comput. Biol. Chem.*, 2025, 108683.

7 A. Nordberg, Mechanisms behind the neuroprotective actions of cholinesterase inhibitors in Alzheimer disease, *Alzheimer Dis. Assoc. Disord.*, 2006, **20**, S12–S18.

8 M. J. Henstra, E. P. Jansma, N. van der Velde, E. L. Swart, M. L. Stek and D. Rhebergen, Acetylcholinesterase inhibitors for electroconvulsive therapy-induced cognitive side effects: a systematic review, *Int. J. Geriatr. Psychiatr.*, 2017, **32**(5), 522–531.

9 K. Tiwari, Comparative Analysis of Oral *versus* Topical Carbonic Anhydrase Inhibitors in Controlling Intraocular Pressure in Glaucoma Patients with Chronic Kidney Disease, *Int. J. Life Sci. Biotechnol. Pharma Res.*, 2025, **14**(5), 1325–1329.

10 C. T. Supuran, Multi-and polypharmacology of carbonic anhydrase inhibitors, *Pharmacol. Rev.*, 2025, **77**(1), 100004.

11 E. R. Swenson, A. Kumar, N. Kumar, and B. V. Alvarez, Targeting Carbonic Anhydrases in Cardiovascular and Pulmonary Disease, *The Carbonic Anhydrases: Current and Emerging Therapeutic Targets*, Springer, 2021, pp. 37–77.

12 L. Ciccone, C. Cerri, S. Nencetti and E. Orlandini, Carbonic anhydrase inhibitors and epilepsy: State of the art and future perspectives, *Molecules*, 2021, **26**(21), 6380.

13 D. I. Kaufman and D. I. Friedman, Should acetazolamide be the first-line treatment for patients with idiopathic intracranial hypertension?, *J. Neuro Ophthalmol.*, 2017, **37**(2), 182–186.

14 E. R. Swenson, Carbonic anhydrase inhibitors and high altitude illnesses, *Carbonic Anhydrase: Mechanism, Regulation, Links to Disease, and Industrial Applications* (2013) 361–386.

15 C. Öztürk, E. Kalay, S. Gerni, N. Balci, F. S. Tokali, O. N. Aslan and E. Polat, Sulfonamide derivatives with benzothiazole scaffold: Synthesis and carbonic anhydrase I–II inhibition properties, *Biotechnol. Appl. Biochem.*, 2024, **71**(1), 223–231.

16 D. Häussinger and W. Gerok, Hepatic urea synthesis and pH regulation: role of CO$_2$, HCO$^-_3$, pH and the activity of carbonic anhydrase, *Eur. J. Biochem.*, 1985, **152**(2), 381–386.

17 S. H. Koenig and R. D. Brown Iii, H2CO3 as substrate for carbonic anhydrase in the dehydration of HCO3, *Proc. Natl. Acad. Sci.*, 1972, **69**(9), 2422–2425.

18 S. Hallaj, W. S. Shalaby, S. Sinha, J. S. Myers and R. Razeghinejad, Systemic Carbonic Anhydrase Inhibitors in Common Ophthalmic Diseases: A Scoping Review from A Clinical Standpoint, *Curr. Ophthalmol. Rep.*, 2025, **13**(1), 9.

19 F. S. Tokalı, Z. Alım and Ü. Yırtıcı, Carboxylate-and Sulfonate-Containing Quinazolin-4 (3H)-one Rings: Synthesis, Characterization, and Carbonic Anhydrase I–II and Acetylcholinesterase Inhibition Properties, *ChemistrySelect*, 2023, **8**(8), e202204191.

20 T. H. Maren, C. W. Conroy, G. C. Wynns and D. R. Godman, Renal and cerebrospinal fluid formation pharmacology of a high molecular weight carbonic anhydrase inhibitor, *J. Pharmacol. Exp. Ther.*, 1997, **280**(1), 98–104.

21 E. Canepa, R. Parodi-Rullan, R. Vazquez-Torres, B. Gamallo-Lana, R. Guzman-Hernandez, N. L. Lemon, F. Angiulli, L. Debure, M. A. Ilies and L. Østergaard, FDA-approved carbonic anhydrase inhibitors reduce amyloid β pathology and improve cognition, by ameliorating cerebrovascular health and glial fitness, *Alzheimer's Dement.*, 2023, **19**(11), 5048–5073.

22 M. I. Hassan, B. Shajee, A. Waheed, F. Ahmad and W. S. Sly, Structure, function and applications of carbonic anhydrase isozymes, *Bioorg. Med. Chem.*, 2013, **21**(6), 1570–1582.

23 S. P. Sterrett, K. L. Penniston, J. S. Wolf Jr and S. Y. Nakada, Acetazolamide is an effective adjunct for urinary alkalization in patients with uric acid and cystine stone formation recalcitrant to potassium citrate, *Urology*, 2008, **72**(2), 278–281.

24 K. H. Lee, U. J. Kim, B. H. Lee and M. Cha, Safeguarding the brain from oxidative damage, *Free Radic. Biol. Med.*, 2025, **226**, 143–157.

25 D.-M. Trofin, D.-P. Sardaru, D. Trofin, I. Onu, A. Tutu, A. Onu, C. Onită, A. I. Galaction and D. V. Matei, Oxidative stress in brain function, *Antioxidants*, 2025, **14**(3), 297.

26 F. R. Buccellato, M. D'Anca, C. Fenoglio, E. Scarpini and D. Galimberti, Role of oxidative damage in Alzheimer's disease and neurodegeneration: From pathogenic mechanisms to biomarker discovery, *Antioxidants*, 2021, **10**(9), 1353.

27 F. Franzoni, G. Scarfò, S. Guidotti, J. Fusi, M. Asomov and C. Pruneti, Oxidative stress and cognitive decline: the neuroprotective role of natural antioxidants, *Front. Neurosci.*, 2021, **15**, 729757.

28 R. B. Semwal, D. K. Semwal, S. Combrinck and A. Viljoen, Health benefits of chromones: Common ingredients of our daily diet, *Phytochem. Rev.*, 2020, **19**(4), 761–785.

29 N. u. A. Mohsin, M. Irfan, S. u. Hassan and U. Saleem, Current strategies in development of new chromone derivatives with diversified pharmacological activities: A review, *Pharm. Chem. J.*, 2020, **54**(3), 241–257.

30 H. Madhav, E. Jameel, M. Rehan and N. Hoda, Recent advancements in chromone as a privileged scaffold towards the development of small molecules for neurodegenerative therapeutics, *RSC Med. Chem.*, 2022, **13**(3), 258–279.

31 A. Simakov, S. Chhor, L. Ismaili and H. Martin, Nrf2 Activation and Antioxidant Properties of Chromone-Containing MTDLs for Alzheimer's Disease Treatment, *Molecules*, 2025, **30**(9), 2048.

32 A. M. Serry, O. M. Abdelhafez, W. K. B. Khalil, K. A. Hamed, M. I. Mabrouk, M. B. Shalaby and E. Y. Ahmed, *In vitro* and *in vivo* antidiabetic evaluation of new Coumarin and Chromone derivatives: Design, synthesis and molecular modeling, *Bioorg. Chem.*, 2025, **159**, 108338.

33 M. Qin, T. Xing, M. Zhang, J. Han, S. Yu, J. Chen and Y. Ma, Synthesis and anti-inflammatory activity of chromone-sulfonamide derivatives as COXs/iNOS dual-target inhibitors, *Med. Chem. Res.*, 2025, **34**(3), 638–647.

34 N. Filipović, T. Balić, M. Medvidović-Kosanović, D. Goman, B. Marković, D. Tatar, S. Roca and K. Mišković Špoljarić, Chromone-Based Copper (II) Complexes as Potential Antitumour Agents: Synthesis, Chemical Characterisation and *In Vitro* Biological Evaluation, *Crystals*, 2025, **15**(5), 389.

35 G. D. Rajesh, M. Vidya, K. Pankaj and K. Abhishek, Design and *in silico* evaluation of oxadiazole linked chromone derivatives as anti-depressant agents, *Res. J. Chem. Environ*, 2024, **28**(1), 73–79.

36 S. Sharma, V. Sharma, G. Singh, H. Kaur, S. Srivastava and M. P. S. Ishar, 2-(chromon-3-yl) imidazole derivatives as potential antimicrobial agents: Synthesis, biological evaluation and molecular docking studies, *J. Chem. Ecol.*, 2017, **10**(1), 35–44.

37 A. O. Jaiyeola, K. Anand, K. Kasumbwe, M. Ramesh and R. M. Gengan, Catalytic synthesis of α-amino chromone phosphonates and their antimicrobial, toxicity and potential HIV-1 RT inhibitors based on silico screening, *J. Photochem. Photobiol., B*, 2017, **166**, 136–147.

38 G. R. Newkome and D. L. Fishel, Synthesis of simple hydrazones of carbonyl compounds by an exchange reaction, *J. Org. Chem.*, 1966, **31**(3), 677–681.

39 A. Xing, P. Zhu, B. Zhang, J. Lu, Y. Zhang, D. Zeng, X. Li and J. Yuan, Synthesis, anticancer and antioxidant activities of novel heterocyclic phenolic hydrazone based derivatives: Investigation of DFT calculation, molecular docking and drug-likeness studies, *J. Mol. Struct.*, 2025, **1319**, 139523.

40 T. Z. Abolibda, M. Fathalla, G. F. Aljohani, E. M. Zayed and S. M. Gomha, Synthesis and *in silico* antiviral activity of novel bioactive thiobarbituric acid based hydrazones and pyrazoles against SARS-CoV-2 main protease (Mpro), *Polycycl. Aromat. Compd.*, 2023, **43**(8), 7635–7650.

41 V. Valcheva, R. Simeonova, M. Mileva, S. Philipov, R. Petrova, S. Dimitrov, A. Georgieva, E. Tsvetanova, Y. Teneva and V. T. Angelova, In Vivo Toxicity, Redox-Modulating Capacity and Intestinal Permeability of Novel Aroylhydrazone Derivatives as Anti-Tuberculosis Agents, *Pharmaceutics*, 2022, **15**(1), 79.

42 M. Kondeva-Burdina, E. Mateev, B. Angelov, V. Tzankova and M. Georgieva, *In silico* evaluation and *in vitro* determination of neuroprotective and MAO-B inhibitory effects of pyrrole-based hydrazones: A therapeutic approach to Parkinson's disease, *Molecules*, 2022, **27**(23), 8485.

43 A. Ibezim, M. N. Ofokansi, X. Ndukwe, C. S. Chiama, B. C. Obi, O. N. Isiogugu, P. E. Ikechukwu, A. M. Onwuka, S. A. Ihim and J. N. Asegbeloyin, Evaluation of anti-malarial potency of new pyrazole-hydrazine coupled to Schiff base derivatives, *Malar. J.*, 2022, **21**(1), 243.

44 T. M. de Aquino, P. H. B. França, É. E. E. S. Rodrigues, I. J. S. Nascimento, P. F. S. Santos-Júnior, P. G. V. Aquino, M. S. Santos, A. C. Queiroz, M. V. Araújo and M. S. Alexandre-Moreira, Synthesis, antileishmanial activity and *in silico* studies of Aminoguanidine Hydrazones (AGH) and Thiosemicarbazones (TSC) against Leishmania chagasi amastigotes, *Med. Chem.*, 2022, **18**(2), 151–169.

45 P. Singh and R. K. Singh, Synthesis of Hydrazone Derivatives and In-silico docking studies against JNK protein to assess anticonvulsant activity of synthesized derivatives, *J. Pharmaceut. Sci. Res.*, 2020, **12**(6), 770–779.

46 H. Ünver, B. Berber, R. Demirel and A. T. Koparal, Design, synthesis, anti-proliferative, anti-microbial, anti-angiogenic activity and *in silico* analysis of novel hydrazone derivatives, *Anti Cancer Agents Med. Chem.*, 2019, **19**(13), 1658–1669.

47 K. Kucukoglu, H. I. Gul, P. Taslimi, I. Gulcin and C. T. Supuran, Investigation of inhibitory properties of some hydrazone compounds on hCA I, hCA II and AChE enzymes, *Bioorg. Chem.*, 2019, **86**, 316–321.

48 N. S. Hari Narayana Moorthy, N. S. Cerqueira, M. J. Ramos and P. A. Fernandes, QSAR analysis of 2-benzoxazolyl hydrazone derivatives for anticancer activity and its possible target prediction, *Med. Chem. Res.*, 2012, **21**(2), 133–144.

49 F. S. Tokalı, P. Taslimi, T. Taskin-Tok, A. Karakuş, N. Sadeghian and İ. Gulçin, Novel hydrazones derived from anthranilic acid as potent cholinesterases and α-glycosidase inhibitors: Synthesis, characterization, and biological effects, *J. Biochem. Mol. Toxicol.*, 2024, **38**(1), e23521.

50 E. Hacıosmanoğlu-Aldoğan, F. Çakır, H. İ. Yetke, F. S. Tokalı and H. Şenol, Synthesis, Characterization, and *In Vitro* and *In Silico* Studies of Substituted-Vanillin Hydrazones of Anthranilic Acid and Their Quinazolin-4 (3H)-One Analogues as Anti Breast Cancer Agents, *ChemistrySelect*, 2025, **10**(3), e202404806.

51 O. Özbek, E. Kalay, A. Cetin, Ö. Isildak, F. Sinan Tokalı, O. Nuri Aslan and I. Isildak, Synthesis and potentiometric sensor applications of a hydrazone derivative molecule: fast and selective determination of cobalt (II) ions, *ChemistrySelect*, 2022, **7**(28), e202201307.

52 E. Kalay, I. N. Korkmaz, F. N. Kacı, O. N. Aslan, P. Güller, F. S. Tokalı and R. Kalın, Design, synthesis, and biological studies of isoniazid-based hydrazone Derivatives: Antibacterial, anticancer, and enzyme inhibitory properties, *Arch. Biochem. Biophys.*, 2025, 110450.

53 F. S. Tokalı, H. Şenol, H. İ. Yetke and E. Hacıosmanoğlu-Aldoğan, Novel quinazoline–chromene hybrids as anticancer agents: Synthesis, biological activity, molecular docking, dynamics and ADME studies, *Arch. Pharmazie*, 2023, **356**(11), 2300423.

54 F. S. Tokalı, H. Şenol, Ş. Ateşoğlu, P. Tokalı and F. Akbaş, Exploring highly selective polymethoxy fenamate isosteres as novel anti-prostate cancer agents: Synthesis, biological activity, molecular docking, molecular dynamics, and ADME studies, *J. Mol. Struct.*, 2025, **1319**, 139519.

55 M. D. Altıntop, A. Özdemir, G. Turan-Zitouni, S. Ilgın, Ö. Atlı, G. İşcan and Z. A. Kaplancıklı, Synthesis and biological evaluation of some hydrazone derivatives as new anticandidal and anticancer agents, *Eur. J. Med. Chem.*, 2012, **58**, 299–307.